The Astrophysical Journal, 792:114 (27pp), 2014 September 10 doi:10.1088/0004-637X/792/2/114

CLUSTER CANDIDATES AROUND LOW-POWER RADIO GALAXIES AT $z \sim 1$–2 IN COSMOS

G. Castignani[1], M. Chiaberge[2,3,4], A. Celotti[1,5,6], C. Norman[2,7], and G. De Zotti[1,8]
[1] SISSA, Via Bonomea 265, I-34136 Trieste, Italy; castigna@sissa.it
[2] Space Telescope Science Institute, 3700 San Martin Drive, Baltimore, MD 21218, USA
[3] INAF-IRA, Via P. Gobetti 101, I-40129 Bologna, Italy
[4] Center for Astrophysical Sciences, Johns Hopkins University, 3400 North Charles Street, Baltimore, MD 21218, USA
[5] INAF-Oservatorio Astronomico di Brera, via Bianchi 46, I-23807 Merate, Italy
[6] INFN-Sezione di Trieste, via Valerio 2, I-34127 Trieste, Italy
[7] Department of Physics and Astronomy, Johns Hopkins University, Baltimore, MD 21218, USA
[8] INAF-Osservatorio Astronomico di Padova, Vicolo dell'Osservatorio 5, I-35122 Padova, Italy
Received 2014 February 4; accepted 2014 June 19; published 2014 August 22

ABSTRACT

We search for high-redshift ($z \sim 1$–2) galaxy clusters using low power radio galaxies (FR I) as beacons and our newly developed Poisson probability method based on photometric redshift information and galaxy number counts. We use a sample of 32 FR Is within the Cosmic Evolution Survey (COSMOS) field from the Chiaberge et al. catalog. We derive a reliable subsample of 21 bona fide low luminosity radio galaxies (LLRGs) and a subsample of 11 high luminosity radio galaxies (HLRGs), on the basis of photometric redshift information and NRAO VLA Sky Survey radio fluxes. The LLRGs are selected to have 1.4 GHz rest frame luminosities lower than the fiducial FR I/FR II divide. This also allows us to estimate the comoving space density of sources with $L_{1.4} \simeq 10^{32.3}$ erg s^{-1} Hz^{-1} at $z \simeq 1.1$, which strengthens the case for a strong cosmological evolution of these sources. In the fields of the LLRGs and HLRGs we find evidence that 14 and 8 of them reside in rich groups or galaxy clusters, respectively. Thus, overdensities are found around $\sim$70% of the FR Is, independently of the considered subsample. This rate is in agreement with the fraction found for low redshift FR Is and it is significantly higher than that for FR IIs at all redshifts. Although our method is primarily introduced for the COSMOS survey, it may be applied to both present and future wide field surveys such as Sloan Digital Sky Survey Stripe 82, LSST, and *Euclid*. Furthermore, cluster candidates found with our method are excellent targets for next generation space telescopes such as *James Webb Space Telescope*.

Key words: galaxies: active – galaxies: clusters: general – galaxies: high-redshift

Online-only material: color figures

1. INTRODUCTION

Clusters of galaxies are among the most massive large-scale structures in the universe. They form from gravitational collapse of matter concentrations induced by perturbations of the primordial density field (Peebles 1993; Peacock 1999). Galaxy clusters have been extensively studied to understand how large-scale structures form and evolve during cosmic time, from galactic to cluster scales (see Kravtsov & Borgani 2012 for a review).

Despite this, the properties of the cluster galaxy population and their changes with redshift in terms of galaxy morphologies, types, masses, colors (e.g., Bassett et al. 2013; McIntosh et al. 2014), and star formation content (e.g., Zeimann et al. 2012, 2013; Santos et al. 2013; Strazzullo et al. 2013; Gobat et al. 2013; Casasola et al. 2013; Brodwin et al. 2013; Alberts et al. 2014) are still debated, especially at redshifts $z \gtrsim 1.5$.

It is also unknown when the intracluster medium (ICM) virializes and starts emitting in X-rays and upscattering the cosmic microwave background through the Sunyaev–Zel'dovich (SZ) effect (Sunyaev & Zel'dovich 1972). See Rosati et al. (2002) for a review. In general, the formation history of the large-scale structures and the halo assembly history (e.g., Sheth & Tormen 2004; Dalal et al. 2008; Adami et al. 2013) are not fully understood.

High-redshift cluster counts are used to constrain cosmological parameters (e.g., Planck Collaboration XX 2013) and to test the validity of the ΛCDM scenario and quintessence models (Jee et al. 2011; Mortonson et al. 2011; Benson et al. 2013). Cluster counts are strongly sensitive to the equation of state of the universe, especially at $z \gtrsim 1$ (Mohr 2005), when the universe starts accelerating and the dark energy component starts becoming dominant. The SZ effect, weak lensing measurements (Rozo et al. 2010), X-ray scaling relations, and data (Vikhlinin et al. 2009; Mantz et al. 2010) are used to evaluate the mass, the redshift of the clusters, and their mass function. Moreover, high-redshift cluster samples might be used to test the (non-)Gaussianity of the primordial density field and to test alternative theories beyond general relativity (see Allen et al. 2011; Weinberg et al. 2013, and references therein for a review).

Searching for high-redshift $z \gtrsim 1$ galaxy clusters is therefore a fundamental issue of modern astrophysics to understand open problems of extra-galactic astrophysics and cosmology from both observational and theoretical perspectives.

An increasing number of high-redshift $z \gtrsim 1$ spectroscopic confirmations of cluster candidates have been obtained in the last years. To the best of our knowledge, in the literature there are only 11 spectroscopically confirmed $z \gtrsim 1.5$ clusters (Papovich et al. 2010; Fassbender et al. 2011; Nastasi et al. 2011; Santos et al. 2011; Gobat et al. 2011; Brodwin et al. 2011, 2012; Zeimann et al. 2012; Stanford et al. 2012; Muzzin et al. 2013; Newman et al. 2014). Only some of them have estimated masses greater than 10^{14} $M_{\odot}$. In addition to them, Tanaka et al. (2013) spectroscopically confirmed a $z = 1.6$ X-ray emitting group, whose estimated mass is 3.2×10^{13} $M_{\odot}$. A $z \sim 1.7$ group associated with a $z \sim 8$ lensed background galaxy was found by Barone-Nugent et al. (2013).

Several methods use photometric and/or spectroscopic redshifts to search for high-redshift overdensities (Eisenhardt et al. 2008; Knobel et al. 2009, 2012; Adami et al. 2010, 2011; George et al. 2011; Wen & Han 2011; Jian et al. 2014). They are generally less effective at $z \gtrsim 1.5$. This is due to the difficulty of obtaining spectroscopic redshift information for a sufficient number of sources at $z > 1$, to the significant photometric redshift uncertainties, and to the small number density of objects.

High-redshift clusters have been searched for by using several other independent techniques, such as, e.g., those that use X-ray emission (e.g., Cruddace et al. 2002; Böhringer et al. 2004; Henry et al. 2006; Šuhada et al. 2012) or the SZ effect (e.g., Planck Collaboration XXIX 2013; Hasselfield et al. 2013; Reichardt et al. 2013). However, such methods require a minimum mass and are rapidly insensitive for detecting $z \gtrsim 1.2$ clusters (see, e.g., discussion in Zeimann et al. 2012). This seems to be true also for the SZ effect.

It is commonly accepted that early-type passively evolving galaxies segregate within the cluster core and represent the majority among the galaxy population, at least at redshifts $z \lesssim 1.4$ (e.g., Menci et al. 2008; Tozzi et al. 2013).

Various methods search for distant clusters taking advantage of the segregation of red objects in the cluster core. Such searches are commonly performed adopting either optical (Gladders & Yee 2005) or infrared (Papovich 2008) color selection criteria. They find a great number of cluster candidates, even at $z \sim 2$ (e.g., Spitler et al. 2012). However, all these methods seem to be less effective at redshifts $z \gtrsim 1.6$. Moreover, such methods require a significant presence of red galaxies. There might be a bias in excluding clusters with a significant amount of star forming galaxies or, at least, in selecting only those overdensities whose galaxies exhibit specific colors (Scoville et al. 2007a; George et al. 2011).

Powerful radio galaxies (i.e., FR IIs; Fanaroff & Riley 1974) have been extensively used for high-redshift cluster searches (e.g., Rigby et al. 2014; Koyama et al. 2014). High-redshift, (i.e., $z \gtrsim 2$) high-power radio galaxies are frequently hosted in Lyα emitting protoclusters (see Miley & De Breuck 2008, for a review). Recently Galametz et al. (2012) and Wylezalek et al. (2013) searched for megaparsec-scale structures around high-redshift (i.e., $z \gtrsim 1.2$), high-power radio galaxies using an infrared (IR) color selection (Papovich 2008).

The radio galaxy population comprises FR I and FR II sources (Fanaroff & Riley 1974). Edge-darkened (FR I) radio galaxies are those where the surface brightness decreases from the core of the source to the lobes or the plumes of the jet at larger scales. Conversely, the surface brightness of edge-brightened (FR II) radio galaxies has its peak at the edges of the radio source.

FR I radio galaxies are intrinsically dim and are more difficult to find at high redshifts than the higher power FR IIs. This has so far limited the environmental study of the high-redshift ($z \gtrsim 1$) radio galaxy population to the FR II class only.

However, due to the steepness of the luminosity function, FR I radio galaxies represent the great majority among the radio galaxy population. Furthermore, on the basis of the radio luminosity function, hints of strong evolution have been observationally suggested by previous work (Sadler et al. 2007; Donoso et al. 2009). Furthermore, their comoving density is expected to reach a maximum around $z \sim 1.0$–1.5 followed by a slow declining at higher redshifts, according to some theoretical models (e.g., Massardi et al. 2010).

At variance with FR II radio galaxies or other types of active galactic nuclei (AGNs), low-redshift FR Is are typically hosted by undisturbed ellipticals or giant ellipticals of cD type (Zirbel 1996), which are often associated with the Brightest Cluster Galaxies (BCGs; von der Linden et al. 2007). Furthermore, FR Is are preferentially found locally in dense environments (Hill & Lilly 1991; Zirbel 1997; Wing & Blanton 2011). This suggests that FR I radio galaxies could be more effective for high-redshift cluster searches than FR IIs.

Chiaberge et al. (2009, hereinafter C09) derived the first sample of $z \sim 1$–2 FR Is within the Cosmic Evolution Survey (COSMOS) field (Scoville et al. 2007b). Chiaberge et al. (2010) suggested the presence of overdensities around three of their highest redshift sources. Based on galaxy number counts, the authors found that the megaparsec-scale environments of these sources are 4σ denser than the mean COSMOS density. Tundo et al. (2012) searched for X-ray emission in the fields of the radio galaxies of the C09 sample. They took advantage of the *Chandra* COSMOS field (C-COSMOS). They did not find any evidence for clear diffuse X-ray emission from the surroundings of the radio galaxies. However, their stacking analysis suggests that, if present, any X-ray emitting hot gas would have temperatures lower than ∼2–3 keV. Furthermore, Baldi et al. (2013) derived accurate photometric redshifts for each of the sources in the Chiaberge et al. (2009) sample.

The goal of this project is to search for high-redshift clusters or groups using FR I radio galaxies as beacons. In this paper we apply the new method we developed to achieve such a goal. The Poisson probability method (PPM) has been introduced in a separate paper (Castignani et al. 2014); it is tailored to the specific properties of the sample (C09) we consider, and it uses photometric redshifts. For comparison, we also apply the Papovich (2008) method that was previously used in other works to search for high-redshift $z \gtrsim 1.2$ cluster candidates (e.g., Galametz et al. 2012; Mayo et al. 2012).

We first redefine the sample by carefully selecting those sources that can be safely considered as low radio power FR Is at $z \sim 1$–2. This is done by estimating the luminosity of each radio galaxy in the sample on the basis of their most accurate photometric redshifts available to date (Baldi et al. 2013) and a careful revision of all adopted radio fluxes.

The main aim of this work is to confirm statistically that the great majority of FR I radio galaxies at ($z \sim 1$–2) reside in dense megaparsec-scale environments, as found at low redshifts. We also discuss the properties of the detected overdensities in terms of their significance, estimated redshift, location, richness, and size, as inferred from the PPM. A careful spectroscopic confirmation of the candidates is however required to have a fully reliable picture of the cluster properties.

In particular, throughout the text we will refer to the megaparsec-scale overdensities as clusters, cluster candidates, and overdensities, with no distinction. However, we keep in mind that these large-scale structures could show different properties and they might be virialized clusters or groups, as well as still forming clusters or protoclusters.

We describe the adopted sample in Section 2, the sample redefinition in Section 3. In Section 4 we estimate the space density of 1.4 GHz sources at $z \sim 1$. We apply our newly developed method to search for overdensities and we discuss the results in Section 5 and Section 6, respectively. In Section 7 we apply the Papovich (2008) method to search for overdensities and we discuss the results. In Section 8 we summarize and discuss our results and the main implications of our findings. In Section 9 we draw conclusions and we outline possible future applications of our work.

Throughout this work we adopt a standard flat ΛCDM cosmology with matter density $\Omega_m = 0.27$ and Hubble constant $H_0 = 71$ km s^{-1} Mpc^{-1} (Hinshaw et al. 2009).

2. THE SAMPLE

The COSMOS survey (Scoville et al. 2007b) is a $1.^{\circ}4 \times 1.^{\circ}4$ equatorial survey that includes multiwavelength imaging and spectroscopy from the radio to the X-ray band. COSMOS is also entirely covered by the Very Large Array Faint Images of the Radio Sky at Twenty-Centimeters (VLA FIRST) survey at 1.4 GHz (Becker et al. 1995), and it includes *Hubble Space Telescope* (*HST*) observations (Koekemoer et al. 2007).

Due to its high sensitivity, angular resolution, and wide spectral coverage, COSMOS is suitable to study large-scale structures at high redshifts, with unprecedented accuracy and low cosmic variance.

Hereafter in this work we will refer to low (high) luminosity radio galaxies, i.e., LLRGs (HLRGs). The LLRGs will denote those radio galaxies with radio power typical of FR Is, while the HLRGs will denote radio galaxies with radio powers generally higher than the FR I/FR II radio power divide ($L_{1.4\,\mathrm{GHz}} \sim 4 \times 10^{32}$ erg s^{-1} Hz^{-1}; Fanaroff & Riley 1974).[9] This does not imply that the LLRGs are FR Is and the HLRGs are FR IIs, especially at high redshift. This is because the HLRGs of our sample have radio powers only slightly higher than those typical of local FR Is. In fact, all sources in our sample (including the HLRGs) have radio powers about ∼2 orders of magnitude lower than those typical of high-z radio galaxies ($z \gtrsim 2$, Miley & De Breuck 2008). Furthermore, both LLRGs and HLRGs might include radio galaxies of transitional type. Therefore, despite the radio galaxies in our sample not clearly exhibiting all properties typical of local FR Is, we will refer to both LLRGs and the HLRGs as FR I radio galaxies, except where otherwise specified.

C09 searched for FR I candidates at $1 \lesssim z \lesssim 2$ in the COSMOS field using multiwavelength selection criteria. Here, we briefly summarize the main steps of the procedure, while more details are given in C09.

The two basic assumptions are: (1) the FR I/FR II divide in radio power per unit frequency (set at $L_{1.4\,\mathrm{GHz}} \sim 4 \times 10^{32}$ erg s^{-1} Hz^{-1}) does not change with redshift; (2) the magnitudes and colors of the FR I hosts at $1 < z < 2$ are similar to those of FR IIs within the same redshift bin, as in the case of local radio galaxies (e.g., Zirbel 1996; Donzelli et al. 2007). Note that the photometric redshifts are affected by great uncertainties, so they do not constitute a selection criterion. In the following, we summarize the source selection procedure adopted by C09.

1. FIRST radio sources in the COSMOS field whose observed 1.4 GHz fluxes are in the range expected for FR Is at $1 < z < 2$ ($1 < F_{1.4} < 13$ mJy) are considered.
2. Sources with FR II radio morphology, i.e., showing clear edge-brightened radio structures, are rejected.
3. Those with bright optical counterparts ($m_{\mathrm{i,Vega}} < 21$) are then excluded since they are likely lower redshift galaxies with radio emission produced by, e.g., starbursts. Note also that this constraint assumes that the magnitude of the FR Is hosts are similar to those of FR IIs.
4. u-band dropouts are rejected as they are likely Lyman-break galaxies at $z > 2.5$ (Giavalisco 2002).

[9] See Sections 3.4 and 3.5 for robust definitions of the two classes concerning our sample.

The selection of the radio sources is based mainly on a flux requirement, criterion (1). The following ones (2, 3, 4) are used only to discard spurious sources from the sample.

The source COSMOS-FR I 236, tentatively classified in C09 as a QSO, was later identified with a known QSO at the spectroscopic redshift $z = 2.132$ (Prescott et al. 2006). Similar to what was done for all sources in our sample (see Sections 3.4 and 3.5), we estimate that the total radio power of this source is 1.96×10^{33} erg s^{-1} Hz^{-1}, based on its redshift and FIRST radio flux of 7.10 mJy (see Baldi et al. 2013). We also assume a radio spectral index $\alpha = 0.8$ (see Section 3.3). Therefore, since this is typical of high-power FR IIs and radio-loud QSOs, we do not consider this source in this paper. Steepening the radio spectrum, i.e., increasing the value of the spectral index α, would increase the estimated radio power, reinforcing our conclusions. Hence, our sample is comprised of 36 sources. Note that the sample, as for any flux-limited one, is affected by the well-known Malmquist bias and thus includes higher/lower power radio sources at high/low redshifts (see Sections 3.4 and 3.5).

As the aim of this work is to search for clusters of galaxies in the fields of the low-power radio galaxies of the C09 catalog, in the following section we redefine the sample by selecting only bona fide low luminosity objects, based on the latest photometric (or spectroscopic, when available) redshift estimates. While we cannot exclude that the remaining (high-power) sources are associated with a dense environment, we will consider them separately.

Hereinafter, we will refer to our sources using the ID number only, as opposed to the complete name COSMOS-FR I nnn.

3. SAMPLE REDEFINITION

The aim of this section is to derive a reliable sample of LLRGs that, based on the information available to date, have $L_{1.4\,\mathrm{GHz}}$ lower than the fiducial separation between FR Is and FR IIs. In order to do so, we require robust measurements of the total radio fluxes, accurate photometric redshifts (in absence of firm spectroscopic redshifts) and assumptions on the K-correction.

3.1. Radio Fluxes

As discussed above, the C09 sample was selected using the radio fluxes from the FIRST survey (Becker et al. 1995) which was performed by using the VLA B-configuration at 1.4 GHz and it covers 10,000 square degrees of the North and South Galactic Caps. The COSMOS field entirely resides within the area mapped by FIRST. Post-pipeline radio maps have a resolution of ∼5 arcsec. The detection limit of the FIRST catalog is ∼1 mJy with a typical rms of 0.15 mJy. When we make use of the FIRST survey, we adopt the flux densities from the catalog as of 2011 October 10. However, the FIRST radio maps may be missing a substantial fraction of any extended low surface brightness radio emission from the lobes of our radio sources, which are close to the detection limit. This is particularly important because of the relatively high angular resolution provided by the VLA configuration used, which is more suitable for detecting compact or unresolved radio sources.

While being slightly shallower than FIRST, the NRAO VLA Sky Survey (NVSS) survey (Condon et al. 1998) may be more suitable for our purposes, since it was obtained by using the VLA-D configuration at 1.4 GHz. The angular resolution of the NVSS radio maps is 45 arcsec (FWHM). Thus, it is more suitable for detecting extended emission of the sources in our

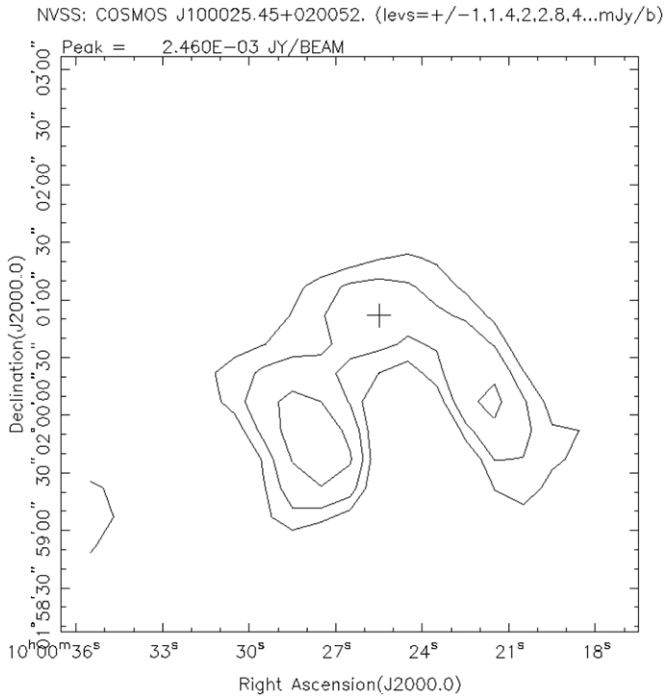

Figure 1. NVSS map, field of 05. The cross marks the coordinates of the radio source.

sample. Therefore, in order to derive the total radio luminosity of our sources, we use the NVSS fluxes and upper limits (as of 2011 October 10), when possible. In the NVSS catalog[10] at the coordinates of the C09 objects, we find 26 of the 36 sources.

While the FIRST survey is complete down to a flux of 1 mJy, the completeness of the NVSS catalog is only 50% at its formal limit of 2.5 mJy, while it rises rapidly to 99% at 3.4 mJy (Condon et al. 1998). Thus, the drawbacks of using NVSS sources are as follows: (1) sources with total radio flux <3.4 mJy might not be included. (2) The identification of the NVSS counterpart of each source is not trivial. Due to the lower angular resolution rms uncertainties are about 7 arcsec at the NVSS limit, as affected by confusion. Furthermore, the extended radio morphology of many of the radio sources might be complex. Therefore, since NVSS is more sensitive to the extended emission than FIRST, the centroid of the FIRST source could not coincide with that in the NVSS map. Also note that, even if the limit of the NVSS catalog is set at 2.5 mJy, some of our fainter sources are detected in the radio maps.

To overcome these inconveniences, we use FIRST (Becker et al. 1995) and VLA COSMOS (Schinnerer et al. 2007). FIRST has a flux density threshold of 1 mJy and a positional accuracy of $\lesssim$1 arcsec for radio pointlike sources. VLA COSMOS has an angular resolution of $1\farcs5 \times 1\farcs4$ and a sensitivity limit of 45 μJy beam^{-1}. It is therefore deeper and with higher angular resolution than FIRST. For the majority of the objects it is straightforward to identify the radio sources in the above surveys. The few cases in which the identification is problematic are discussed in the following.

For these cases we consider the VLA COSMOS maps to clearly identify the radio sources, as described in the following for source 05. In Figure 1 we show the NVSS radio map of the field around object 05. Visual inspection reveals the presence of a complex radio morphology, which might be (erroneously) identified with either the narrow-angle tail (e.g., NGC 1265, O'Dea & Owen 1986) or the wide-angle tail (e.g., 3C 465; Venturi et al. 1995) radio morphology. The NVSS catalog reports sources at distances of ∼60 and ∼67 arcsec to the SW and SE from the VLA-COSMOS coordinates of source 05, and fluxes of 3.4 and 3.7 mJy, respectively. A third radio source located at the position of 05 is visible in the map, but it is below the threshold of the NVSS catalog.

In Figure 2 (left) we show the same field as seen with VLA-COSMOS, at a much higher angular resolution. Such image shows the presence of a number of point-like sources and some extended emission. In the right panel we report the *HST* image of the same field, taken with the Advanced Camera for Surveys (ACS) and the F814W filter, as part of the COSMOS survey. The radio contours from VLA-COSMOS are overplotted in yellow. It is clear that the radio sources seen in VLA-COSMOS overlap with foreground galaxies. This generates the complex extended emission seen in the NVSS map. By using higher resolution radio data and the optical image, we are able to overcome the confusion problem in the NVSS map. The NVSS catalog misses our source and detects only the two unrelated brighter radio emitting regions.

Similarly, other sources have extended radio morphology, as is clear from visual inspection of the NVSS maps. The angular separation between the coordinates reported in the NVSS catalog and those obtained by using VLA-COSMOS is about ∼15 arcsec. This is the case with sources 26, 52, 202, 224, and 228, where such angular separations are 15.37, 16.4, 12.82, 12.43, and 18.52 arcsec, respectively. In Figure 3 we report the NVSS fields of 26 and 224 as examples. These sources show a radio morphology similar to that of 05. However, a bright source is clearly present in each of these two fields, very close to the radio galaxy. They are merged in the NVSS map in a single structure due to the low NVSS angular resolution.

We consider the radio NVSS maps of all eight sources that are not present in the NVSS catalog. We visually inspect each map and search for the presence of radio contours centered around the position of the radio source. For five out of the eight, we find evidence of a radio source located at the coordinates of the radio galaxy. This is the case with sources 11, 20, 22, 27, and 39, where the radio contours are consistent with a radio flux close to the NVSS formal limit of 2.5 mJy. In Figure 4 we report the fields of 22 and 39 as examples. Being very close to or below the formal completeness limit, we expect that possible systematics might occur in the flux measurements. Therefore, we adopt a fiducial 2.5 mJy upper limit for all eight sources which are not included in the NVSS catalog.

The fiducial FIRST and NVSS flux uncertainties for the sources in our sample are within ∼0.1–0.2 mJy and ∼0.4–0.6 mJy, respectively. However, we prefer not to report the flux uncertainty associated with each source. This is because we are considering fluxes down to the completeness limit of both the FIRST and the NVSS surveys and, therefore, the flux uncertainties might be underestimated.

3.2. Redshifts

We adopt accurate photometric redshifts derived by Baldi et al. (2013, hereinafter B13) through a careful analysis of the spectral energy distribution (SED) of the host galaxies. As mentioned in Section 2, throughout this paper we adopt the photometric redshifts derived in B13, which we specifically focus on in the sample considered here. These photometric redshifts have a great advantage with respect to those in

[10] http://www.cv.nrao.edu/nvss/

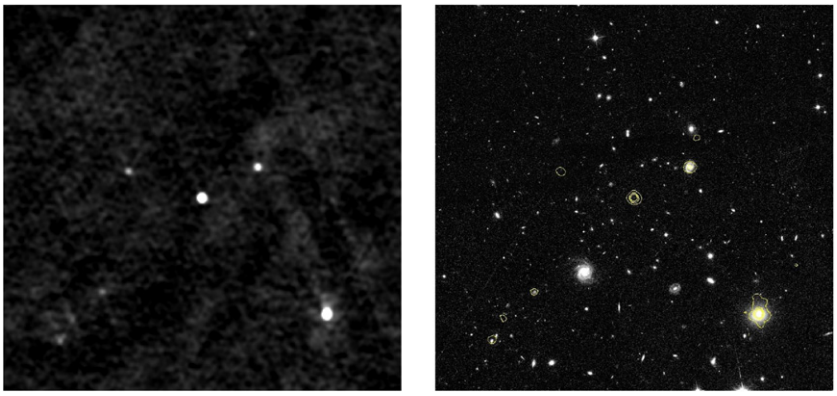

Figure 2. Field ($3' \times 3'$ dimension) of 05. Left: VLA-COSMOS map. Right: *HST* image taken from ACS and the F814W filter. Yellow contours are from VLA-COSMOS. The angular scale is the same for both of the panels.

(A color version of this figure is available in the online journal.)

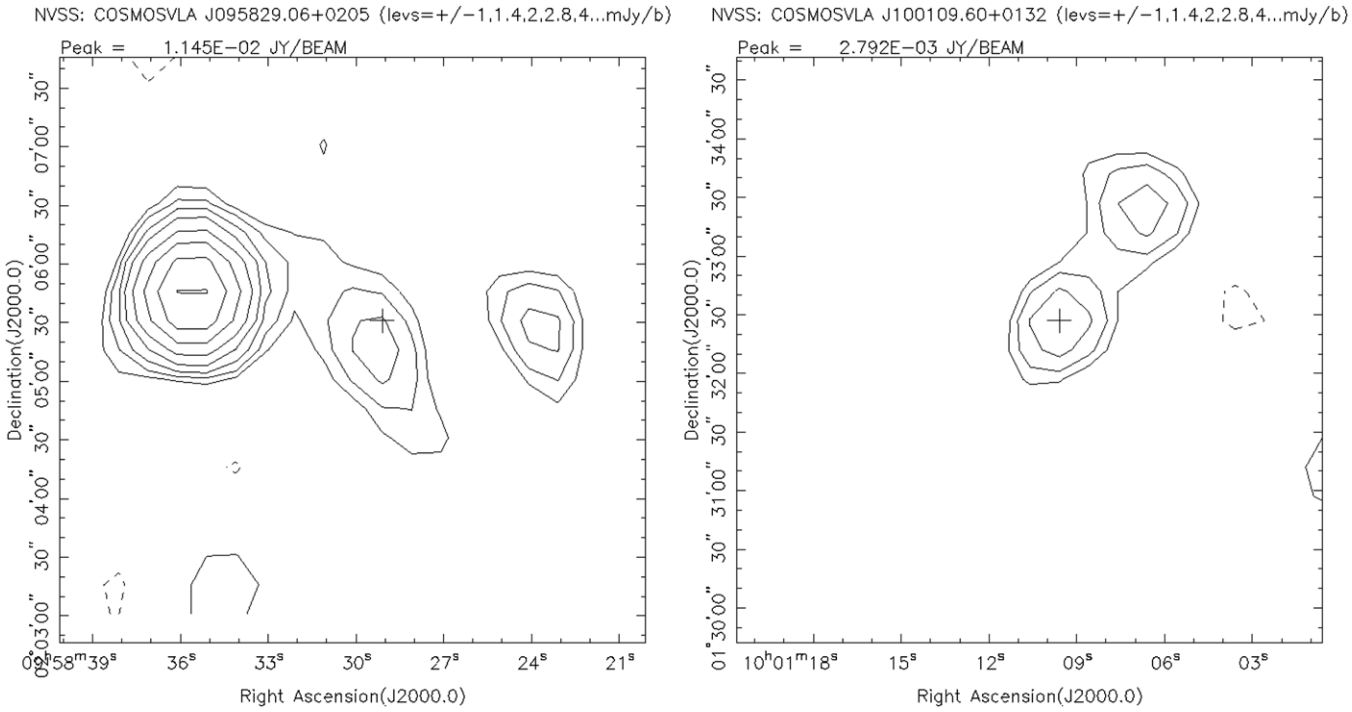

Figure 3. NVSS maps. The cross marks the coordinates of the radio source. Left: field of 26. Right: field of 224.

Mobasher et al. (2007) and Ilbert et al. (2009, hereinafter I09), which were automatically derived by using the COSMOS photometric catalogs.

I09 estimated photometric redshifts by using the photometric data points from 30 bands for those sources with $I < 25$ in in the deep Subaru area of the COSMOS field (Taniguchi et al. 2007). B13 carefully identified the optical counterparts of the radio sources in all of the photometric bands. The authors discovered that, in a few cases, sources in different bands were misidentified in the COSMOS source list, therefore leading to erroneous photometric redshift estimates. B13 also performed a more refined SED modeling, with the inclusion of two stellar populations. At variance with the I09 catalog, B13 considered only broad band photometric data and excluded narrow and medium band data, which can be strongly contaminated by emission lines that are not included in the stellar templates.

We also search for the spectroscopic redshift of our sources in the zCOSMOS-bright (Lilly et al. 2007) and MAGELLAN (Trump et al. 2007) catalogs. Only 7 out of the 36 sources in our sample are found.

In agreement with B13, we do not use the spectroscopic redshift for object 25. This is because of its clear misidentification in the MAGELLAN catalog (see Section 6.1 in B13). Therefore, for the great majority of the sources we have to rely on photometric redshifts.

The redshifts of three (namely, 27, 52, and 66) out of the seven sources for which spectroscopic redshifts are available are significantly outside the $z \sim 1$–2 range of C09 selection. Therefore, we exclude them from the sample. Redshifts $z = 0.2847$ and $z = 0.7417$ are reported in the MAGELLAN catalog for sources 27 and 52, respectively. The redshifts reported for source 66 in the MAGELLAN and the zCOSMOS-bright catalog are consistent with each other and equal to $z = 0.6838$ and $z = 0.6803$, respectively. Searching for cluster candidates at intermediate or low redshifts (i.e., $z \lesssim 0.8$) is not the aim of this project. Therefore, we naturally reject sources 27, 52, and

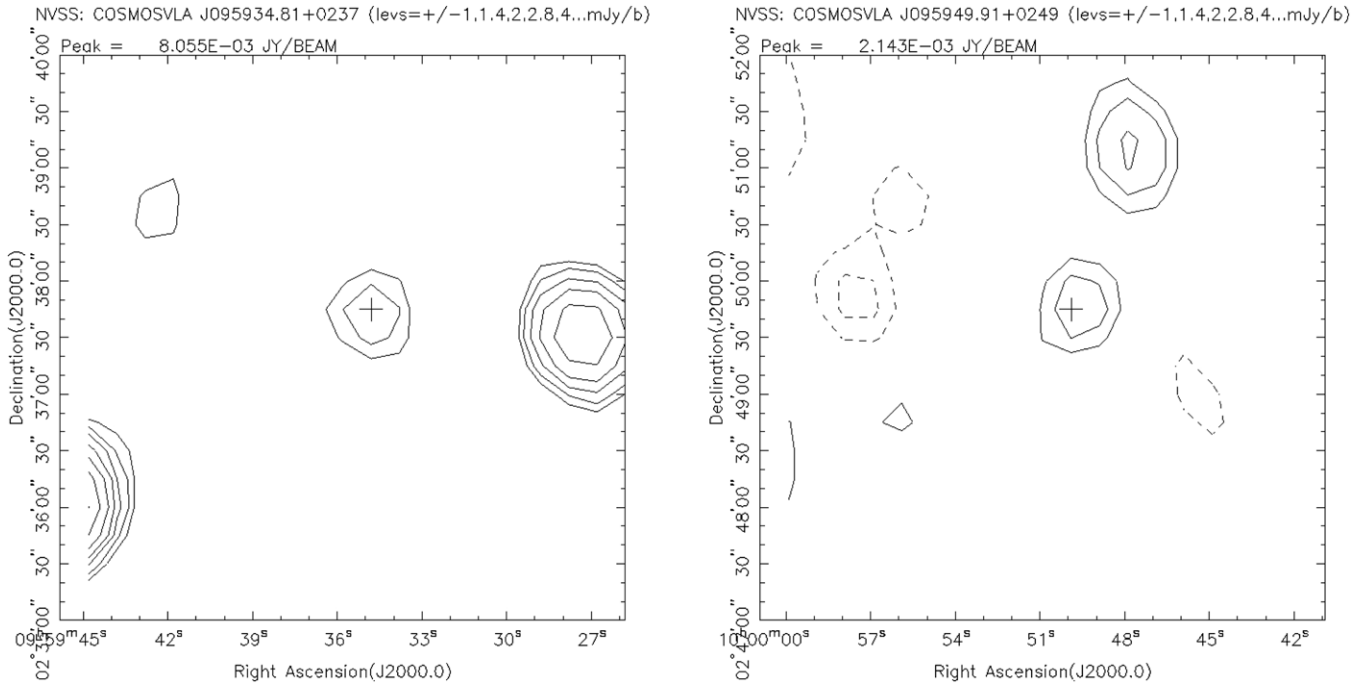

Figure 4. NVSS maps. The cross marks the coordinates of the radio source. Left: field of 22. Right: field of 39. Examples of sources not included in the NVSS catalog, but clearly present in the NVSS maps. Their 1.4 GHz fluxes are close to the NVSS 2.5 mJy limit.

66, which are all located at $z \leqslant 0.75$. We also exclude source 07 from the sample because it is a peculiar radio source (as suggested in Baldi et al. 2013). It might be an FR II radio galaxy at significantly high redshift. It will be studied in a forthcoming paper. Conversely, we do not exclude those sources (e.g., 28 and 32) that have a photometric redshift formally above $z \sim 2$. This is because, even if they are at redshifts well outside the fiducial range of our interest, they were not rejected during the C09 selection. Therefore, they could have similar properties to those of the other galaxies in our sample. Furthermore, since such sources populate the high-redshift tail of our sample, their megaparsec-scale environments are still worth investigating (see also Section 7 for further discussion about source 28).

Summarizing, with respect to the original list given in C09, we reject sources 07, 27, 52, and 66 (in addition to 236, the QSO we already discussed above). The sample is thus reduced to 32 objects.

3.3. Rest Frame Radio Luminosities

In agreement with C09, we assume that the radio spectrum in the region around 1.4 GHz is a power law of the form $S_\nu \propto \nu^{-\alpha}$, where S_ν is the radio flux density at the observed frequency ν, and α is the spectral index assumed to be $\alpha = 0.8$, according to C09. Such an assumption requires that the flat ($\alpha \sim 0$) radio emission of the core is negligible with respect to the extended emission (jets and lobes) in the considered spectral range. This is formally correct at the lowest radio frequencies, but it is less certain at higher frequencies. However, since the radio data do not allow us to separate the emission of our sources into different components, we assume that the measured flux at 1.4 GHz is dominated by extended emission. If $\alpha = 0.3$ instead of 0.8, the luminosity would increase by only a factor of <1.8, for the worst case of a source at $z = 2$.

Thus the isotropic rest frame 1.4 GHz luminosity density is given by:

$$L_{1.4} = 4\pi S_{1.4} D_L(z)^2 (1+z)^{\alpha-1}, \quad (1)$$

where $S_{1.4}$ is the observed flux density at 1.4 GHz and D_L is the luminosity distance.

3.4. The Low Luminosity Radio Galaxy Subsample

In Figure 5 (left panel) we report the luminosity versus redshift scatterplot. The lower/upper thick black lines in the plot are the FIRST sample selection lower/upper boundaries adopted in C09 (1.0 mJy and 13.0 mJy, respectively). Since NVSS fluxes are in general higher than FIRST fluxes, we expect all sources to lie above the lower line.

Since we are interested in searching for clusters around FR Is, we consider the 1.4 GHz luminosity intervals spanned for each source, within the redshift uncertainties, for an assigned 1.4 GHz radio flux.

Therefore, we conservatively select only those sources whose 1.4 GHz luminosity intervals lie entirely below the FR I/FR II radio luminosity divide of 4×10^{32} erg s^{-1} Hz^{-1}. According to this criterion, we select 21 bona fide LLRGs, whose redshifts span the range $z = 0.88$–1.33 and have radio luminosities between $L_{1.4} = (0.84$–$3.24) \times 10^{32}$ erg s^{-1} Hz^{-1}. In Figure 5 (right panel) we plot the scatterplot focused on the LLRGs only. The median redshift and 1.4 GHz luminosity of the LLRGs are $z_{\rm median} = 1.1$ and $L_{1.4,\rm median} = 1.84 \times 10^{32}$ erg s^{-1} Hz^{-1}, respectively. For comparison, radio galaxies of similar power, selected within the 3C catalog, span a much smaller redshift range. Chiaberge et al. (1999) report a range $z = 0.0037$–0.29 and a median value $z = 0.03$ for their sample of 33 FR Is.

The LLRGs span a limited range of luminosity and slightly broader range of redshift. However, because of the steepness of the radio luminosity function, most sources are at $z \sim 1$.

Being at relatively low redshifts, these objects and their megaparsec-scale environment can be studied in greater detail than the whole sample of FR I candidates considered in this work. This is mainly because COSMOS field number densities are much higher and statistical photometric redshift uncertainties are smaller than at higher redshifts (Ilbert et al. 2009).

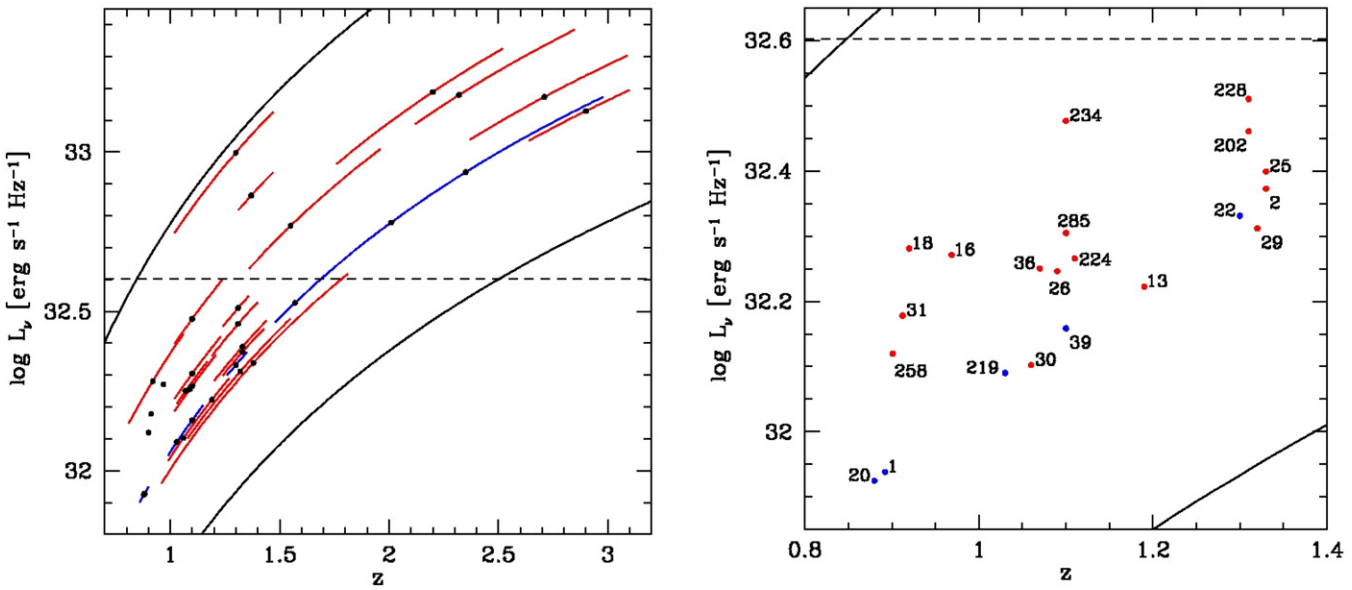

Figure 5. Left: luminosity vs. redshift scatterplot. Red lines correspond to sources with an NVSS counterpart and fluxes. Blue lines correspond to upper limits at 2.5 mJy flux for the sources with no NVSS flux. Solid black lines: FIRST cut at 1 mJy, 13 mJy; The blue and the red lines indicate the uncertainties on the photometric redshift. The x and y values of the dots are the redshift and the luminosity of each source, respectively. Dots that are not associated with lines show the objects with spectroscopic redshifts. Horizontal dashed line: FR I/FR II luminosity divide, assumed to be constant with redshift. Right: LLRGs only. Color legend is the same as for the left panel. Each dot represents a source, identified by the corresponding ID number.

(A color version of this figure is available in the online journal.)

Furthermore, spectroscopic redshift information is available for some of the LLRGs only and photometric redshifts from B13 are more accurate for the LLRGs than for the HLRGs, with the latter, on average, being at higher redshifts.

Therefore we separate the LLRGs from the remaining sources, that are generally at higher luminosities and redshifts than the HLRGs. In particular, the photometric redshifts of the LLRGs are better constrained, since the typical statistical uncertainty dramatically increases above $z \sim 1.3$ (see, e.g., Figure 9 in I09) and because all of the sources in our sample with spectroscopic redshifts belong to the LLRG class.

3.5. The High Luminosity Radio Galaxy Subsample

We consider in this section the remaining sources in the sample, i.e., the HLRGs, that do not belong to the LLRG subclass. Note that the radio morphology of both LLRGs and the HLRGs is not of FR II type. In fact, sources with a clear FR II morphology have been rejected as part of the original sample selection in C09. Furthermore, the cosmological evolution of the FR I/FR II radio divide is still unknown, i.e., high-z FR I sources might have higher radio power than those of local FR Is, as suggested by Heywood et al. (2007).

This makes the nature of these HLRGs very unclear and deserving investigation. In the following, we consider the HLRGs separately from the rest of the sample (i.e., the LLRGs) in order to avoid any bias due to possible differences in the megaparsec-scale environments of low and high luminosity sources.

We find 11 HLRGs. Their redshifts and radio luminosities span the intervals $z = 1.30$–2.90 and $L_{1.4} = (2.18$–$15.44) \times 10^{32}$ erg s^{-1} Hz^{-1}, respectively. The median redshift and luminosity are $z_{\rm median} = 2.01$, $L_{1.4,\rm median} = 8.64 \times 10^{32}$ erg s^{-1} Hz^{-1}, respectively.

3.6. Statistical Properties

In Table 1 we summarize the properties of the sources in our sample, separating them between the LLRGs (top) and the HLRGs (bottom). We refer to C09 and their Table 1 for more details about the sample. In Figure 6 we report the radio power distribution for our sample obtained by considering NVSS fluxes (left panel) and FIRST fluxes (right panel). Limited to this section only, we also consider the FIRST instead of the NVSS radio powers only. This is because FIRST fluxes are available for all sources in our sample, while this is not the case for NVSS.

The averages of the logarithmic FIRST and NVSS luminosities of the sources in our sample are $\log[L_{1.4,\rm FIRST}/(\rm erg\ s^{-1}\ Hz^{-1})] = 32.32 \pm 0.41$ and $\log[L_{1.4,\rm NVSS}/(\rm erg\ s^{-1}\ Hz^{-1})] = 32.47 \pm 0.37$, respectively, where the reported uncertainties are the rms dispersions around the averages. This shows that the sources in our sample have, on average, 1.4 GHz radio luminosities slightly below the FR I/FR II radio luminosity divide and that this result is independent of the two different sets of radio fluxes adopted (i.e., FIRST or NVSS). However, the logarithmic difference between the FIRST and NVSS luminosities for the sources in our sample is, on average, $\langle \log(L_{1.4,\rm NVSS}/L_{1.4,\rm FIRST}) \rangle = 0.15$ and the rms dispersion around the average is 0.14 dex. This can be translated into the fact that, on average, the 1.4 GHz luminosities estimated from the NVSS fluxes are 1.5 times than those estimated by adopting FIRST fluxes.

Therefore, NVSS are slightly higher than FIRST luminosities for the FR Is in our sample. This suggests that the NVSS survey is more sensitive to extended emission and it might be more effective than FIRST to estimate the true radio luminosity of our sources.

We test the presence of bimodality in both the FIRST and NVSS radio power distributions by applying the KMM algorithm described in Ashman et al. (1994). The KMM test assumes that the considered distributions are Gaussian functions or a sum of them. We find that the luminosity distribution is strongly inconsistent with being unimodal at 99.75% confidence level (i.e., more than 3σ) if the NVSS fluxes (or upper limits) are adopted. If we adopt the FIRST fluxes for those sources

Table 1
Sample Properties

ID	R.A. (deg)	Decl. (deg)	Redshift	FIRST Flux (mJy)	NVSS Flux (mJy)	$L_{1.4\,\mathrm{GHz}}$ (10^{32} erg s^{-1} Hz^{-1})	Radio Morphology
The Low Luminosity Radio Galaxy Subsample							
COSMOS FR I 01	150.20744	2.2818749	0.8823[a]–0.8827[b]	1.06	—	0.85	Compact
COSMOS FR I 02	150.46751	2.7598829	$1.33\pm^{0.10}_{0.09}$	2.25	2.6	2.36	Extended
COSMOS FR I 13	149.97784	2.5042069	$1.19\pm^{0.08}_{0.11}$	1.50	2.4	1.67	Compact
COSMOS FR I 16	150.53772	2.2673550	0.9687[a]	5.70	4.4	1.87	Unresolved
COSMOS FR I 18	149.69325	2.2674670	$0.92\pm^{0.14}_{0.11}$	4.39	5.1	1.91	Extended
COSMOS FR I 20	149.83209	2.5695460	$0.88\pm^{0.02}_{0.02}$	1.33	—	0.84	Extended
COSMOS FR I 22	149.89508	2.6292144	$1.30\pm^{0.05}_{0.04}$	2.74	—	2.14	Compact
COSMOS FR I 25	150.45673	2.5597000	$1.33\pm^{0.11}_{0.13}$	2.18	2.7	2.45	Compact
COSMOS FR I 26	149.62114	2.0919881	$1.09\pm^{0.12}_{0.07}$	1.88	3.2	1.80	Extended
COSMOS FR I 29	149.64587	1.9529760	$1.32\pm^{0.23}_{0.24}$	2.13	2.3	2.05	Compact
COSMOS FR I 30	149.61542	1.9910541	$1.06\pm^{0.11}_{0.07}$	1.26	2.4	1.27	Compact
COSMOS FR I 31	149.61916	1.9163600	0.9123[a]–0.9132[b]	3.71	4.1	1.51	Compact
COSMOS FR I 36	150.55662	1.7913361	$1.07\pm^{0.10}_{0.04}$	3.19	3.3	1.78	Unresolved
COSMOS FR I 39	149.95804	2.8288901	$1.10\pm^{0.05}_{0.05}$	1.37	—	1.44	Compact
COSMOS FR I 202	149.99506	1.6324950	$1.31\pm^{0.09}_{0.12}$	1.08	3.3	2.89	Extended
COSMOS FR I 219	150.06444	2.8754051	$1.03\pm^{0.02}_{0.04}$	1.85	—	1.23	Compact
COSMOS FR I 224	150.28999	1.5408180	$1.10\pm^{0.10}_{0.04}$	3.31	3.2	1.84	Extended
COSMOS FR I 228	149.49455	2.5052481	$1.31\pm^{0.05}_{0.07}$	2.04	3.7	3.24	Compact
COSMOS FR I 234	150.78925	2.4539680	$1.10\pm^{0.14}_{0.08}$	4.43	5.2	3.00	Extended
COSMOS FR I 258	149.55934	1.6310670	0.9009[b]	2.24	3.7	1.32	Compact
COSMOS FR I 285	150.72131	1.5823840	$1.10\pm^{0.13}_{0.08}$	2.95	3.5	2.02	Extended
The High Luminosity Radio Galaxy Subsample							
COSMOS FR I 03	150.00253	2.2586310	$2.20\pm^{0.32}_{0.44}$	4.21	5.2	15.44	Unresolved
COSMOS FR I 04	149.99153	2.3027799	$1.37\pm^{0.10}_{0.06}$	5.99	7.5	7.30	Extended
COSMOS FR I 05	150.10612	2.0144780	$2.01\pm^{0.22}_{0.35}$	1.30	—	6.01	Compact
COSMOS FR I 11	150.07816	1.8985500	$1.57\pm^{0.14}_{0.09}$	1.13	—	3.36	Compact
COSMOS FR I 28	149.60064	2.0918673	$2.90\pm^{0.20}_{0.26}$	1.77	2.4	13.46	Compact
COSMOS FR I 32	149.66830	1.8379777	$2.71\pm^{0.38}_{0.34}$	1.39	3.1	14.88	Compact
COSMOS FR I 34	150.56023	2.5861051	$1.55\pm^{0.41}_{0.19}$	5.25	4.5	5.87	Unresolved
COSMOS FR I 37	150.74336	2.1705379	$1.38\pm^{0.43}_{0.42}$	1.87	2.2	2.18	Compact
COSMOS FR I 38	150.53645	2.6842549	$1.30\pm^{0.17}_{0.28}$	10.01	11.6	9.95	Compact
COSMOS FR I 70	150.61987	2.2894360	$2.32\pm^{0.53}_{0.20}$	3.90	4.5	15.10	Compact
COSMOS FR I 226	150.43864	1.5934480	$2.35\pm^{0.63}_{0.31}$	1.25	—	8.64	Compact

Notes. Column description: (1) source ID number; (2) R.A.J2000 [degree]; (3) Decl.J2000 [degree]; (4) Redshifts. Photometric from B13 and spectroscopic from either MAGELLAN (Trump et al. 2007) or zCOSMOS-bright (Lilly et al. 2007) catalogs are denoted with the superscript a or b, respectively; (5) 1.4 GHz FIRST fluxes [mJy]; (6) 1.4 GHz NVSS fluxes [mJy]. We assume 2.5 mJy flux (reported as—in the table) for those sources that are not in the NVSS catalog; (7) 1.4 GHz radio power [10^{32} erg s^{-1} Hz^{-1}]. NVSS flux or 2.5 mJy upper limit adopted. Radio spectrum assumed: $L_\nu \propto \nu^{-\alpha}$, $\alpha = 0.8$; (8) radio morphology as in C09.

for which we have the NVSS upper limits we find that the unimodality is rejected at 70.10% confidence level (i.e., just above 1σ). The unimodality is rejected at a level less than 1σ (i.e., 63.88%) if the FIRST fluxes are instead considered for all sources.

The presence of bimodality in the NVSS radio power distribution of the FR Is in our sample suggests that the HLRGs might be drawn from a different parent population. However, the bimodality disappears when the FIRST fluxes are included. Furthermore, the Gaussian approximation is a strong assumption and it might not correspond to our case. Therefore, even if we find evidence of bimodality in the radio power distribution, we cannot draw firm conclusions.

4. SOURCE SPACE DENSITY

The careful selection of our sample and the accurate photometric redshifts make possible a reliable estimate of the space density of 1.4 GHz sources at $z \simeq 1$, albeit in a narrow luminosity range. For this purpose we consider a flux-limited sample with NVSS flux density brighter than 2.5 mJy. Most (13 out of 19) sources are in the redshift and luminosity ranges $0.9 \leqslant z \leqslant 1.4$ and $10^{32.11} \leqslant L_{1.4}/\mathrm{erg\ s^{-1}\ Hz^{-1}} \leqslant 10^{32.51}$. Their median redshift and radio luminosity are $z_{\mathrm{median}} = 1.1$ and $L_{1.4\,\mathrm{median}} = 10^{32.30}$ erg s^{-1} Hz^{-1}, respectively. Only for these is there sufficient statistics to get a meaningful estimate of the space density.

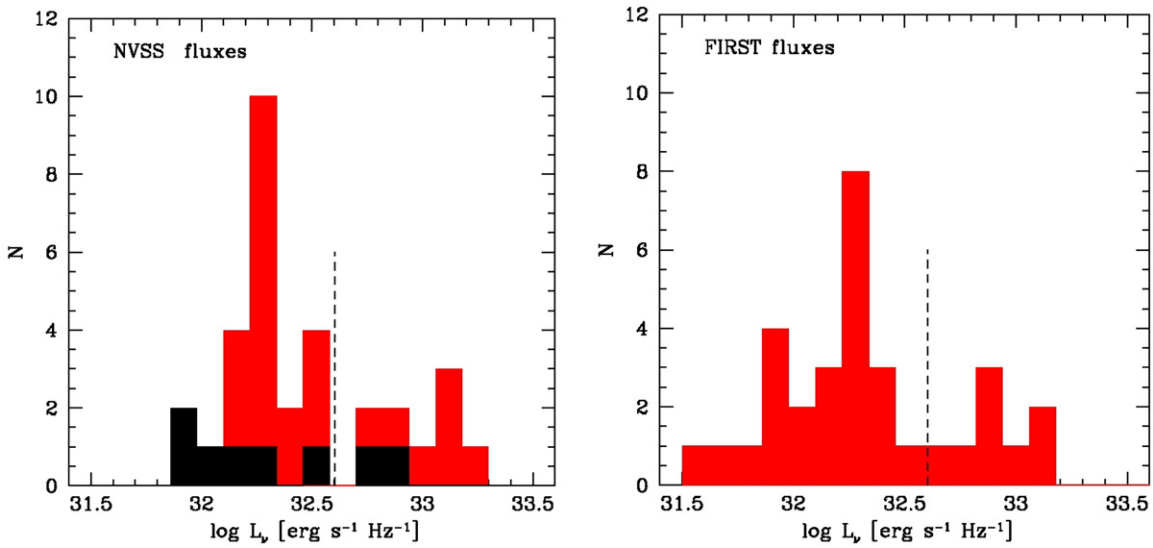

Figure 6. 1.4 GHz luminosity histograms for the whole sample. The vertical dashed line is the FR I/FR II radio power divide. Left: NVSS fluxes adopted. The black regions refer to sources with no NVSS flux, for which a fiducial 2.5 mJy upper limit is assumed. Right: FIRST fluxes adopted.

(A color version of this figure is available in the online journal.)

The NVSS catalogue is 50% complete for unresolved sources with corrected flux density of 2.5 mJy, although its completeness rises rapidly to 99% at 3.4 mJy (Condon et al. 1998). To correct for the incompleteness of our sample we have exploited the FIRST survey, estimated to be 95% complete down to 2 mJy. In our field there are three FIRST sources within the considered luminosity and redshift ranges, not present in the NVSS catalog. Only one of them (i.e., source 22) has a FIRST flux density $\geqslant$2.5 mJy. We have added it to sample.

Using the classical $1/V_{\rm max}$ estimator (Schmidt 1968) we get a comoving density of $(6.09^{+1.97}_{-1.77})\,10^{-6}$ Mpc^{-3} $(d\log L)^{-1}$. The positive error also takes into account the possibility that the other two FIRST sources not present in the NVSS catalog are above the 2.5 mJy limit if observed with the larger NVSS beam. Then, the fractional positive error due to incompleteness would be $2/14 \simeq 0.14$; we have added it in quadrature to the Poisson error.

A further uncertainty is due to errors on photometric redshifts that may have moved some sources unduly in or out of the chosen redshift range. To estimate this uncertainty we have generated $N = 1,000$ simulated samples, randomly assigning to each of the 20 sources in the flux-limited sample (including the FIRST source) a redshift randomly drawn from a distribution made of two half-Gaussians with mean equal to the estimated photometric redshift and dispersions equal to the positive and negative 1σ redshift errors. For each simulated sample we have derived the comoving space density with the $1/V_{\rm max}$ estimator, finding $(5.4 \pm 0.4)\,10^{-6}$ Mpc^{-3} $(d\log L)^{-1}$, where the errors correspond to the range encompassing 68% of the distribution. Then, these errors have been added in quadrature to those estimated above. This leads to our final estimate for the comoving space density: $(5.4^{+2.0}_{-1.8})\,10^{-6}$ Mpc^{-3} $(d\log L)^{-1}$.

In Figure 7 we compare our estimate (open square) of the comoving space density of 1.4 GHz radio sources with $L_{1.4} \simeq 10^{32.3}$ erg s^{-1} Hz^{-1} and $z \simeq 1.1$ with results found in literature for different redshifts. Our result is somewhat higher than that by Smolčić et al. (2009, see their Table 2) at a similar redshift. It is also higher than expected from the model by Willott et al. (2001), but consistent with predictions by Massardi et al. (2010) and McAlpine et al. (2013).

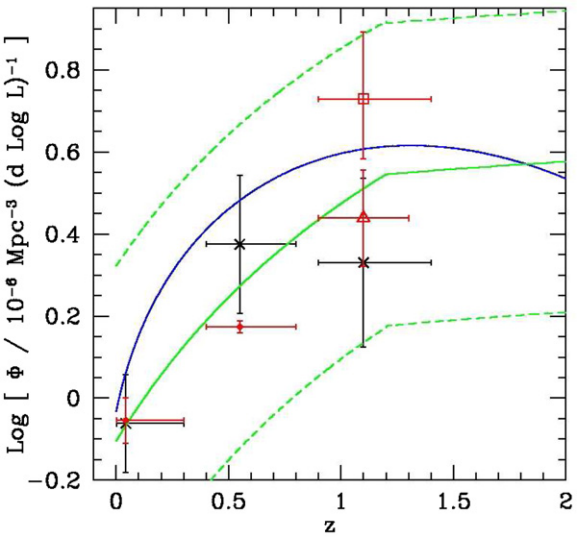

Figure 7. Redshift dependence of the comoving space density of 1.4 GHz radio sources with $L_{1.4} \simeq 10^{32.3}$ erg s^{-1} Hz^{-1}. The red points are observational estimates by Mauch & Sadler (2007) at $z \simeq 0.043$, Donoso et al. (2009) at $z \simeq 0.55$, Smolčić et al. (2009) at $z \sim 1$ (open triangle), and this work (open square). The black points are from the Willott et al. (2001) model, corrected to the cosmology used in this paper. The solid blue line shows the predictions by Massardi et al. (2010) for steep-spectrum radio sources. The green lines refer to the pure luminosity evolution model by McAlpine et al. (2013, model 3 in their Table 3), with its errors. The uncertainties are at 1σ level.

(A color version of this figure is available in the online journal.)

A comparison with comoving space densities of sources with similar luminosities at lower redshifts confirms that they are strongly evolving. We find an enhancement of the density by a factor $6.1^{+2.4}_{-2.2}$ compared with the Mauch & Sadler (2007) estimate at $z \sim 0$, consistent with Rigby et al. (2008) who reported an increase of a factor of 5–9 from $z \sim 0$ to $z \sim 1$ for FR I radio galaxies with $L_{1.4} > 10^{32}$ erg s^{-1} Hz^{-1}.

5. THE POISSON PROBABILITY METHOD (PPM)

Our method for searching for overdensities at $z \sim$ 1–2 has been introduced and extensively discussed in Castignani et al.

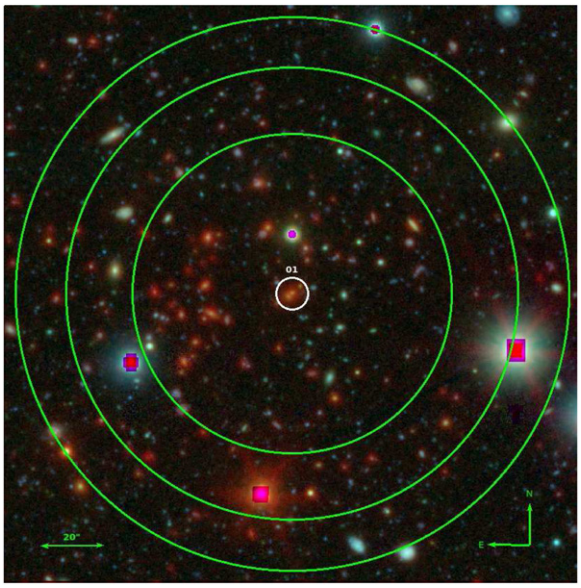

Figure 8. RGB image of the field of 01. The image is obtained using *Spitzer* 3.6 μm, Subaru r$^+$-, and Subaru *B*-band images for the R, G, and B channels, respectively. Green circles show the first three regions of the PPM tessellation. The white circle is centered at the position of the coordinates of the radio source 01.

(A color version of this figure is available in the online journal.)

(2014). The method is based on galaxy number counts and photometric redshifts.

The PPM is adapted from that proposed by Gomez et al. (1997, see their Appendix A) to search for X-ray emitting substructures within clusters. The authors note how their method naturally overcomes the inconvenience of dealing with low number counts per pixel ($\gtrsim$4), which prevent them from applying the standard methods based on χ^2-fitting (e.g., Davis & Mushotzky 1993). Here we are dealing with a similar problem, since the number counts in the fields of the radio galaxies are small (see also Section 8.7.2). In fact the COSMOS field survey has, on average, number densities per unit redshift $dn/dz/d\Omega \simeq$25, 10, and 3 arcmin^{-2} at redshift $z \sim$1, 1.5, and 2.0, respectively (see Ilbert et al. 2009). We refer to Castignani et al. (2014, hereinafter Paper I) for a further discussion and a comprehensive description of the PPM. Here we briefly summarize the basic steps of the procedure.

1. We tessellate the projected space with a circle centered at the coordinates of the beacon (in our specific case this is the location of the FR I radio galaxy) and a number of consecutive adjacent annuli. The regions are concentric and have the same area (2.18 armin^2). In Figure 8 we show the RGB image of the field of 01. The first three regions of the tessellation are shown.
2. For each region, we count galaxies with photometric redshifts from the I09 catalog within a given interval Δz centered at the centroid redshift $z_{\rm centroid}$ for different values of Δz and $z_{\rm centroid}$. The values of Δz and $z_{\rm centroid}$ densely span between 0.02–0.4 and 0.4–4.0, respectively.
3. For each area and for a given redshift bin we calculate the probability of the null hypothesis (i.e., no clustering) to have the observed or a higher number of galaxies, assuming Poisson statistics and the average number count density estimated from the COSMOS field.[11] Starting from the coordinates of the beacon we select only the first consecutive overdense regions for which the probability of the null hypothesis is $\leqslant$30%. We merge the selected regions and we compute the probability, separately, as done for each of them. Then, we estimate the detection significance of the number count excess as the complementary probability. We set it equal to zero, if the annulus closest to the radio galaxy has an innermost radius $r \gtrsim$ 132 arcsec, i.e., we do not consider overdensities that start to be detected at a significant angular separation from the location of the source. This projected distance corresponds to 0.8 h^{-1} Mpc ($h = 0.71$), the scale where the amplitude of the correlation function between Radio Loud AGNs (RLAGNs) and Luminous Red Galaxies (LRGs) is reduced to a few percent ($\sim$4%) of the value at its maximum, up to $z \simeq 0.8$ (e.g., Donoso et al. 2010; Worpel et al. 2013)
4. In Figure 9 we show the resulting plots for some of the sources in our sample. The points in each panel represent the probability estimated for a given choice of the parameters $z_{\rm centroid}$ and Δz. We apply a Gaussian filter to eliminate high frequency noisy patterns. Figure 9 shows the plot where the filter has been applied.
5. We define as overdensities only those regions for which consecutive $\geqslant 2\sigma$ points are present in a region of the PPM plot at least $\delta z_{\rm centroid} = 0.1$ long on the redshift axis $z_{\rm centroid}$ and defined within a tiny $\delta(\Delta z) = 0.01$ wide interval centered at $\Delta z = 0.28$. These values are chosen because of the properties of the errors of the photometric redshifts of our sample and of the size of the Gaussian filter we apply. In particular the redshift bin corresponds to the estimated statistical 2σ photometric redshift uncertainty at $z \sim 1.5$ for dim galaxies (i.e., with AB magnitude i$^+ \sim$ 24, Ilbert et al. 2009). These magnitudes are typical of the galaxies we expect to find in clusters in the redshift range of our interest. We verified that the results are stable with respect to a slightly different choice of the redshift bin Δz. The 2σ threshold is low, but it is equal to that adopted by previous works that searched for high-redshift galaxy clusters (e.g., Durret et al. 2011; Galametz et al. 2012).
6. In order to estimate the significance of each megaparsec-scale overdensity we apply the same procedure outlined in the previous step, but progressively increasing the significance threshold until no overdensity is found. We assign to each overdensity a significance equal to the maximum significance threshold at which the overdensity is still detected. Note that in case the overdensity displays multiple local peaks we do not exclude the lower significance ones.
7. We estimate the redshift of each overdensity as the centroid redshift $z_{\rm centroid}$ at which the overdensity is selected in the PPM plot.
8. We also estimate the size of each overdensity in terms of the minimum and maximum distances from the FR I beacon at which the overdensity is detected. In order to do so we consider all points in the PPM plot within the region centered around $\Delta z = 0.28$ and at least $\delta z_{\rm centroid} = 0.1$ long on the redshift axis $z_{\rm centroid}$ which defines the overdensity. For each of these points the overdensity is detected within

[11] We test if cosmic variance affects our analysis selecting four disjoint quadrants in the COSMOS survey to estimate the field density separately from each quadrant. We verify that the results are independent of the particular choice of the field. We also note that the beacon is not excluded in estimating the number count density.

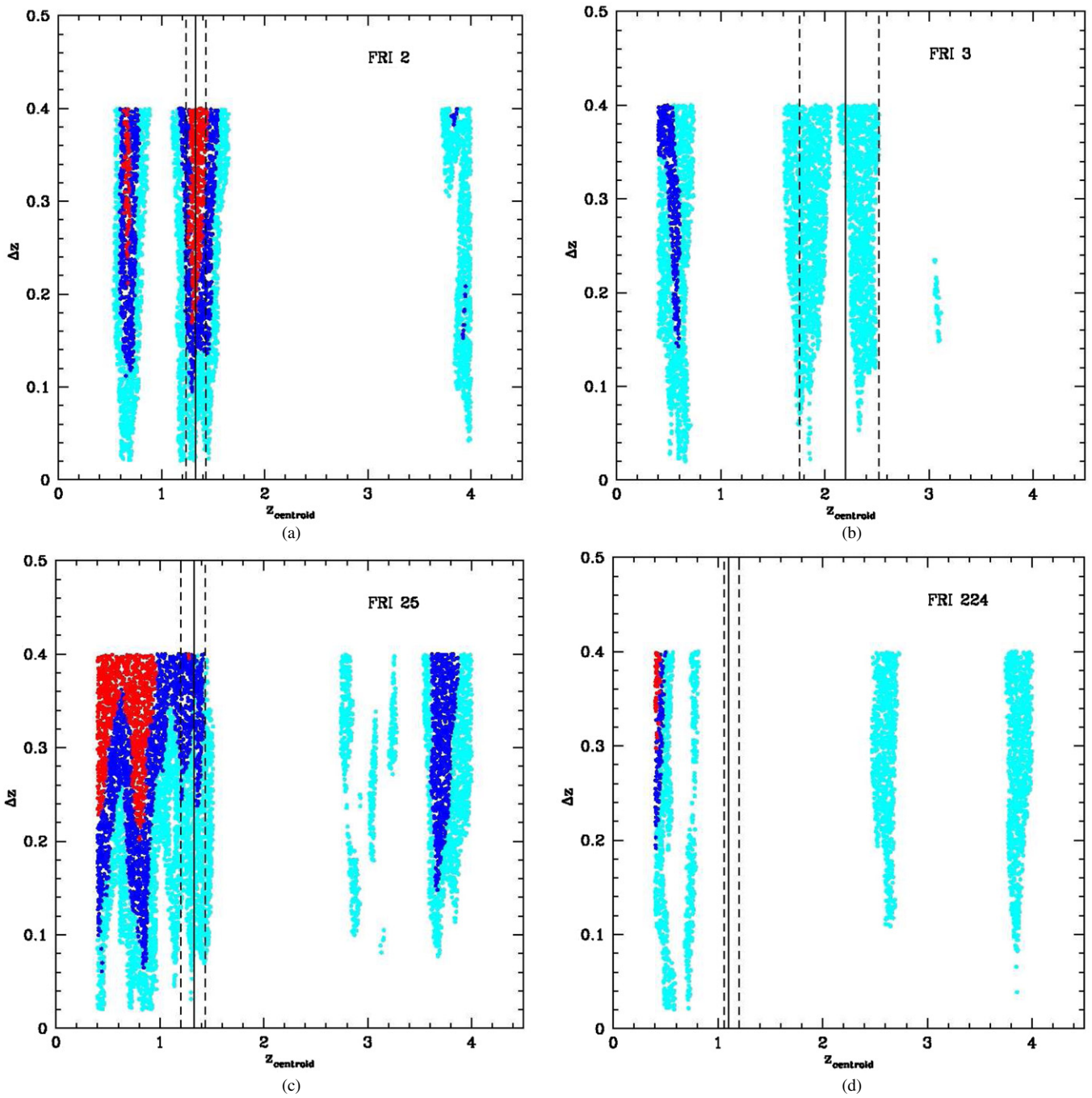

Figure 9. PPM plots for sources (a) 02, (b) 03, (c) 25, and (d) 224. The abscissa of the vertical solid line is at the redshift of the source. The vertical dashed lines show its uncertainties as given in Baldi et al. (2013). We plot only the points corresponding to detected overdensities for different values of Δz and $z_{\rm centroid}$. Color code: $\geqslant 2\sigma$ (cyan points), $\geqslant 3\sigma$ (blue points), $\geqslant 4\sigma$ (red points). A Gaussian filter, which eliminates high frequency noisy patterns, has been applied.

(A color version of this figure is available in the online journal.)

certain minimum and maximum distances. We estimate the minimum and maximum distances of the overdensity as the average (and the median) of the minimum and maximum distances associated with all of these points, respectively. We also compute the rms dispersion of the distances as an estimate for the uncertainty.

9. In order to estimate the fiducial uncertainty for the redshift of the overdensity we consider all sources located within the median minimum and maximum distances from the coordinates of the source within which the overdensity is detected in the projected space. We also limit to the sources that have photometric redshifts within a redshift bin $\Delta z = 0.28$ centered at the estimated redshift of the overdensity. This value is chosen to ensure consistency with the value used for our detection procedure (see above). We estimate the overdensity redshift uncertainty as the rms dispersion of the photometric redshifts of the sources that are selected in the field of the radio galaxy. In particular, if $N \gg 1$ sources were uniformly distributed within the redshift bin $\Delta z = 0.28$ we would obtain an rms dispersion of 0.08. We expect the estimated redshift uncertainty to be around this value.

10. We associate with each radio galaxy any overdensity in its field that is located at a redshift compatible with that of the radio source itself (i.e., when the interval centered at the redshift estimated for the overdensity and with a half-width equal to two times the fiducial redshift error intersects the redshift range defined within the radio galaxy redshift uncertainties). Note that multiple overdensity associations are not excluded.

6. RESULTS

In this section we discuss the results of the PPM. In Figure 9 we show four examples of typical PPM results for fields of the FR Is. In panel (a) we report the PPM plot for the LLRG 02. The photometric redshift of source 02 and that estimated for the overdensity perfectly match. Two other overdensities are detected in the field of 02 at redshifts $z = 0.66$ and 3.94, respectively. They are clearly identified at their estimated redshift by visual inspection of the PPM plot.

Interestingly, the lower redshift cluster is present ($\sim$20 arcsec far from the location of our FR I) in both the $z \lesssim 1$ group catalogs of Knobel et al. (2009, 2012), who estimated a redshift of $z = 0.69$ for the overdensity.

In panel (b) we report a similar example for the $z \sim 2$ HLRG 03. Despite the high photometric uncertainties for this source two distinct overdensities are clearly detected within the redshift uncertainties of source 03 at $z = 1.82$ and 2.39, respectively. Another overdensity is detected at $z = 0.56$, as also clearly identified by visual inspection of the plot. Interestingly, it is present (with an angular offset of $\sim$20 arcsec from the coordinates of our FR I) in the $z \lesssim 1$ group catalogs of Knobel et al. (2009, 2012), who estimated a redshift of $z = 0.66$ for the overdensity.

In panel (c) we report the PPM plot for LLRG 25. A clear overdense (i.e., $\geqslant 2\sigma$) region extends in the PPM plot from $z_{\rm centroid} = 0.40$ to $z_{\rm centroid} = 1.51$. Due to such a large redshift range we interpret the overdense region in the plot as due to a projection effect, where multiple overdensities are present in the field of 25 at different redshifts. Our peak finding procedure detects in fact four overdensities within such a redshift interval, at $z = 0.46$, 0.80, 1.23, and 1.37, respectively. Only the last two redshifts agree with the redshift of the radio galaxy, consistent with our association criterion. The significances of the two overdensities are similar and equal to 2.7σ and 2.8σ, respectively. Therefore, we are confident that these two peaks are associated with the same overdensity. On the contrary, the first two lower redshift overdensities are detected with higher significances of 3.8σ and 4.2σ, respectively. Moreover, since they are detected at redshifts significantly below that of the radio galaxy, we suggest that they are overdensities which are in the field of 25 but they are not associated with the source. In fact, two overdensities are found in the Knobel et al. (2012) group catalog at redshifts of $z = 0.35$ and 0.82 and at angular separations of 8 arcsec and 46 arcsec from the coordinates of source 25, respectively. The fact that the redshifts of the $z \sim 0.4$ overdensity estimated by Knobel et al. (2012) and in this work marginally agree with each other might be due to the fact that, according to our procedure, we consider sources down to $z_{\rm centroid} = 0.4$. Therefore, the inconsistency might be due to a boundary effect that would disappear if we considered lower redshift sources. Note also that we find another clear overdensity in the field of 25 at an estimated redshift of $z = 3.72$. High significance (i.e., $\gtrsim 2\sigma$) patterns are also clearly visible in the PPM plot around $z_{\rm centroid} \sim 3$. According to our selection criteria, they are not detected as overdensities but interpreted as noisy features. This is because they are spiky features that are not stable with respect to different values for the Δz and $z_{\rm centroid}$ parameters.

In panel (d) we show a clear example where no overdensity is found to be associated with radio galaxy 224, although three other overdensities are detected at redshifts $z = 0.46$, 2.58, and 3.88, well outside the redshift range of our interest. No group associated with this field is found within the Knobel et al. (2009, 2012), George et al. (2011) catalogs.

In the following sections we will show our results. In Section 6.1 we will describe our cluster candidate catalog, in Section 6.2 we will discuss the presence of other cluster candidates in the fields of our sample of FR Is that are not associated with our sources. In Sections 6.3 and 6.4 we will discuss the megaparsec-scale environments of the remaining fields and the multiple megaparsec-scale overdensity detections that occur for some of the sources in our sample, respectively. In Section 6.5 we will reconsider our work by rejecting those sources that were masked, classified as stars, or identified as X-ray AGNs in the I09 catalog. In Sections 6.6 and 6.7 we will discuss the projected space information obtained with the PPM, focusing on our cluster size estimates. In Sections 7 and 7.1 we will apply the Papovich (2008) method to our sample and compare the results with those obtained independently by using the PPM, respectively.

6.1. Cluster Candidates

In Table 2 we report the overdensities found in the fields of our sample that are associated with the corresponding sources, according to the PPM procedure. We distinguish between the LLRGs (top table) and the HLRGs (bottom table). We discuss the estimated sizes in Section 6.6. All of the overdensities are robustly detected with respect to slightly different choices of the involved parameters (e.g., a different choice of the redshift bin Δz, a different selection threshold, a different choice in the parameters of the tessellation of the projected space).

According to the overdensity selection procedure outlined in Section 5 we find that 22 out of the 32 sources in our sample are hosted in a dense megaparsec-scale environment. The cluster candidates associated with the sources in the sample have an average redshift of $z_{\rm avg} = 1.41$ with an rms dispersion around the average of 0.55. The median redshift is $z_{\rm median} = 1.31$. When calculating these quantities for the fields in which multiple associations between distinct overdensities and the beacon radio galaxy are identified we only consider the overdensity whose estimated redshift is the closest to that of the radio galaxy.

In particular, we find that 14 radio galaxies out of the 21 LLRGs and 8 out of the 11 HLRGs are associated with overdensities. These correspond to percentages of 67% $\pm$ 10% and 73% $\pm$ 13% for the two subsamples, respectively, where the 1σ uncertainties are estimated according to binomial statistics. These percentages fully agree within the reported errors. Therefore the environments of the two subsamples are statistically indistinguishable. Thus, if we do not distinguish between the two different classes (i.e., the LLRGs and the HLRGs) we find that 22 out of the 32 radio galaxies in our sample (i.e., 69% $\pm$ 8%) are found in dense megaparsec-scale environments.

The overdensity in the field of 16 is not formally associated with the radio galaxy, according to the outlined procedure. However, we do not reject it from Table 2 because it would be included if the photometric redshift of the radio source

Table 2
Cluster Candidates and Their Properties as Inferred with the PPM

ID	$z_{\rm source}$	$z_{\rm overdensity}$	Significance	$r_{\rm min}$ (arcsec)	$r_{\rm max}$ (arcsec)	$r_{\rm max,phys.}$ (kpc)	$r_{\rm max,comov.}$ (kpc)
The Low Luminosity Radio Galaxy Subsample							
01	0.8823[a]–0.8827[b]	0.84 ± 0.07	3.5	0.0 ——	70.7 ——	536 ——	987 ——
02	$1.33\pm^{0.10}_{0.09}$	1.33 ± 0.09	4.3	$19.2\pm^{+24.3}_{-19.2}$ (0.0)	119.3 ± 16.2 (122.5)	1008 ± 136	2349 ± 319
16	0.9687[a]	1.12 ± 0.06	3.5	0.0 ——	100.5 ± 3.3 (100.0)	830 ± 27	1760 ± 57
18	$0.92\pm^{0.14}_{0.11}$	0.80 ± 0.08	5.6	0.0 ——	110.4 ± 25.4 (132.3)	834 ± 191	1501 ± 345
20	$0.88\pm^{0.02}_{0.02}$	0.96 ± 0.06	3.9	0.0 ——	80.4 ± 8.3 (86.6)	637 ± 65	1249 ± 129
22	$1.30\pm^{0.05}_{0.04}$	1.41 ± 0.09	3.3	$20.8\pm^{+24.6}_{-20.8}$ (0.0)	94.2 ± 11.6 (86.6)	800 ± 98	1929 ± 237
25[c]	$1.33\pm^{0.11}_{0.13}$	1.23 ± 0.07	2.8	57.2 ± 9.9 (50.0)	120.9 ± 19.5 (132.3)	1009 ± 162	2250 ± 363
		1.37 ± 0.08	2.7	51.1 ± 4.6 (50.0)	86.6 ——	736 ——	1745 ——
26	$1.09\pm^{0.12}_{0.07}$	1.15 ± 0.07	3.9	42.6 ± 27.4 (50.0)	149.0 ± 12.3 (158.1)	1237 ± 102	2659 ± 219
29	$1.32\pm^{0.23}_{0.24}$	1.34 ± 0.09	2.1	77.5 ± 7.9 (70.7)	120.5 ± 11.2 (122.5)	1020 ± 94	2387 ± 221
36	$1.07\pm^{0.10}_{0.04}$	1.18 ± 0.07	3.0	0.0 ——	82.6 ± 6.9 (86.6)	685 ± 57	1494 ± 124
39	$1.10\pm^{0.05}_{0.05}$	1.27 ± 0.06	3.5	0.0 ——	70.7 ——	597 ——	1356 ——
228	$1.31\pm^{0.05}_{0.07}$	1.17 ± 0.06	3.2	0.0 ——	70.7 ——	588 ——	1276 ——
234[d]	$1.10\pm^{0.14}_{0.08}$	0.93 ± 0.08	2.5	0.0 ——	108.7 ± 8.3 (111.8)	854 ± 65	1649 ± 125
285	$1.10\pm^{0.13}_{0.08}$	1.01 ± 0.07	2.1	50.0 ——	70.7 ——	568 ——	1143 ——
The High Luminosity Radio Galaxy Subsample							
03[c]	$2.20\pm^{0.32}_{0.44}$	1.82 ± 0.08	2.6	0.0 ——	58.7 ± 11.4 (50.0)	502 ± 97	1416 ± 275
		2.39 ± 0.09	2.5	$15.8\pm^{+23.2}_{-15.8}$ (0.0)	74.9 ± 7.0 (70.7)	617 ± 57	2093 ± 195
04	$1.37\pm^{0.10}_{0.06}$	1.57 ± 0.09	2.0	0.0 ——	62.4 ± 10.1 (70.7)	532 ± 86	1368 ± 221
05	$2.01\pm^{0.22}_{0.35}$	1.97 ± 0.07	2.2	0.0 ——	50.0 ——	424 ——	1261 ——
28[c]	$2.90\pm^{0.20}_{0.26}$	2.71 ± 0.07	2.0	86.3 ± 11.0 (86.6)	129.9 ± 4.2 (132.3)	1044 ± 33	3876 ± 125
		2.98 ± 0.09	2.5	0.0 ——	101.0 ± 11.7 (100.0)	793 ± 91	3159 ± 366
34	$1.55\pm^{0.41}_{0.19}$	1.31 ± 0.07	2.7	45.7 ± 27.9 (50.0)	103.6 ± 8.3 (100.0)	871 ± 69	2012 ± 161
37	$1.38\pm^{0.43}_{0.42}$	1.95 ± 0.07	3.0	86.6 ——	121.6 ± 2.9 (122.5)	1035 ± 24	3054 ± 72
38	$1.30\pm^{0.17}_{0.28}$	0.88 ± 0.07	3.7	0.0 ——	90.0 ± 9.4 (86.6)	698 ± 72	1312 ± 137
226	$2.35\pm^{0.63}_{0.31}$	1.99 ± 0.06	2.5	70.5 ± 4.9 (70.7)	107.2 ± 5.8 (111.8)	910 ± 49	2723 ± 147

Notes. Cluster candidates in the fields of the LLRGs (top) and HLRGs (bottom) associated with the corresponding source. Column description: (1) source ID number; (2) photometric redshift of the source along with uncertainties from B13. Spectroscopic redshifts from either MAGELLAN (Trump et al. 2007) or zCOSMOS-bright (Lilly et al. 2007) catalogs are denoted with the superscript [a] or [b], respectively; (3) redshift of the overdensity and corresponding rms dispersion, both estimated with the PPM; (4) significance of the overdensity estimated by the PPM in terms of σ; (5) average minimum radius (arcsec) of the overdensity along with the rms dispersion around the average (both estimated with the PPM). The median value (arcsec) is written between the parentheses; (6) average maximum radius (arcsec) of the overdensity along with its rms dispersion around the average (both estimated with the PPM). The median value (arcsec) is written between the parentheses; (7) average physical size (kpc) of the overdensity along with the rms dispersion; (8) average comoving size (kpc) of the overdensity along with the rms dispersion. The rms dispersions and the median values in Columns 5, 6, 7, and 8 are not reported in those cases where the rms dispersion is null.

[c] Sources 03, 25, 28 are counted twice because multiple peaks are found to be associated with the corresponding radiogalaxies within the photometric redshift uncertainties.

[d] Photometric redshifts from Ilbert et al. (2009) denoted as *zpbest* are adopted. They do not include masked sources, stars, and X-ray AGN.

($z = 0.97^{+0.12}_{-0.07}$, see Table 6 in B13) would be considered instead of the spectroscopic redshift.

Note that, a posteriori, the redshift estimated for each overdensity in the sample is remarkably consistent with that of the source estimated in B13. The overdensity redshift uncertainties are generally small and comparable to typical statistical photometric redshift uncertainties in I09.

As expected, the overdensities associated with the LLRGs are generally at lower redshifts than those of the HLRGs. These lower redshift overdensities are also detected, on average, with higher significances ($\sigma_{\rm avg} = 3.36$) than those associated with the HLRGs ($\sigma_{\rm avg} = 2.64$). This effect is in agreement with that pointed out in Paper I and it is mainly due to both increasing photometric redshift errors and to the smaller number counts that occur for increasing redshifts. If we focus on the overdensities found among the two different subsamples, separately (i.e., the LLRGs and the HLRGs) we find that the average, the rms dispersion around the average, and the median values of the redshifts of the overdensities associated with the LLRGs are $z_{\rm avg} = 1.13$, rms $= 0.20$, and $z_{\rm median} = 1.17$, respectively. The average, the rms dispersion around the average and the median values of the redshifts of the overdensities associated with the HLRGs are $z_{\rm avg} = 1.88$, rms $= 0.65$, and $z_{\rm median} = 1.97$, respectively.

C10 suggested the presence of overdensities around three of our highest redshift sources, namely, sources 03, 05, and 226. Based on galaxy number counts, the authors found that the megaparsec-scale environments of these source are 1.7 times denser with respect to the mean COSMOS density. They translated this into a 4σ overdensity significance. Interestingly,

Table 3
Cluster Candidates not Associated with the Radio Galaxies as Inferred with the PPM

ID	z_{source}	$z_{overdensity}$	Significance	r_{min} (arcsec)	r_{max} (arcsec)	$r_{max,phys.}$ (kpc)	$r_{max,comov.}$ (kpc)
The Low Luminosity Radio Galaxy Subsample							
13	$1.19\pm^{0.08}_{0.11}$	1.42 ± 0.06	3.50	0.0 ——	84.4 ± 8.0 (86.6)	719 ± 68	1741 ± 165
202	$1.31\pm^{0.09}_{0.12}$	0.91 ± 0.08	2.30	$7.6\pm^{17.9}_{7.6}$ (0.0)	114.3 ± 16.6 (122.5)	899 ± 130	1718 ± 249
219	$1.03\pm^{0.02}_{0.04}$	1.20 ± 0.06	2.60	0.0 ——	70.7 ——	589 ——	1297 ——
The High Luminosity Radio Galaxy Subsample							
32	$2.71\pm^{0.38}_{0.34}$	2.22 ± 0.07	2.20	0.0 ——	67.1 ± 7.8 (70.7)	561 ± 65	1808 ± 210

Notes. Cluster candidates in the fields of the LLRGs (top table) and HLRGs (bottom table) not associated with the radio galaxies. Column description: (1) source ID number; (2) photometric redshift of the source along with uncertainties from B13. (3) redshift of the overdensity and corresponding rms dispersion, both estimated with the PPM; (4) significance of the overdensity estimated by the PPM in terms of σ; (5) average minimum radius (arcsec) of the overdensity along with the rms dispersion around the average (both estimated with the PPM). The median value (arcsec) is written between the parentheses; (6) average maximum radius (arcsec) of the overdensity along with its rms dispersion around the average (both estimated with the PPM). The median value (arcsec) is written between the parentheses; (7) average physical size (kpc) of the overdensity along with the rms dispersion; (8) average comoving size (kpc) of the overdensity along with the rms dispersion; The rms dispersions and the median values in Columns 5, 6, 7, 8 are not reported in those cases where the rms dispersion is null.

we find this is in full agreement with our results, since we find that all three sources reside in high significance ($\sim 2.5\sigma$) and high-redshift ($z \simeq 2$) megaparsec-scale overdensities. The cluster candidate associated with our source 03 is also present in the proto-cluster and group catalog of Diener et al. (2013). They estimated a redshift of 2.44, which is in good agreement with our estimate ($z = 2.39$) for one of the two megaparsec-scale overdensities associated with source 03. Spitler et al. (2012) found a cluster candidate that is about ~3.8–5.4 arcmin from source 03. The authors estimated a redshift of $z = 2.2$, on the basis of photometric redshift information. Even if both the redshift and the projected coordinates are only marginally consistent with those of our cluster candidate, it might be possible that the source 03 belongs to the same large-scale cluster structure presented in Spitler et al. (2012). We also report the PPM plot for the field of this source in Figure 9, panel (b). Interestingly, whereas the independent Papovich (2008, see Section 7) method suggests that source 03 is in a $\sim 3.3\sigma$ overdensity, it does not detect any overdensity in the fields of sources 05 and 226. We will discuss this in details in Sections 7.1 and 7.2.

We searched for cluster candidates in catalogs of $z \lesssim 1$ groups in the COSMOS field that were obtained by using spectroscopic redshift information (Knobel et al. 2009, 2012) or photometric redshifts combined with previous X-ray-selected cluster samples (George et al. 2011). Interestingly, five groups in the fields and redshifts of our FR Is are present in these catalogs. These five source are 01, 16, 18, 20, and 31. However, we note that the coordinates reported in Knobel et al. (2012) for the groups and in the fields of 16, 18 and 20 and those of the FR Is are separated by ~63, 40, and 42 arcsec, respectively. Therefore, these three associations are only marginally consistent. Conversely, the offsets for the other two FR Is (i.e., 01 and 31) are $\lesssim 14''$; hence the associations are more robust. Source 258 is the only FR I in our sample with a photometric or spectroscopic redshift less than $z = 1$ for which no group was found in these catalogs. Similarly, the PPM does not find any megaparsec-scale overdensity associated with that source. We also note that the cluster candidate in the field of 01 was previously suggested in Finoguenov et al. (2007).

Redshifts $z = 0.88$, 0.92, 0.79, and 0.96 are reported for the groups associated with sources 01, 16, 18, and 20, respectively (Finoguenov et al. 2007; Knobel et al. 2009, 2012; George et al. 2011). The redshifts fully agree with our estimates obtained with the PPM method (see Table 2) for all these overdensities. A group is also present in the field of our source 31 at an estimated redshift $z = 0.91$ in Knobel et al. (2009). This is exactly the spectroscopic redshift of the FR I. Based on spectroscopic redshifts, Knobel et al. (2009) associated only two members with this group. They also estimated a relatively low mass of $M = 8.9 \times 10^{12}\ M_{\odot}$. The PPM does not find this group. It might be explained by the fact that the PPM is more effective at finding more massive structures, as discussed in Section 8 and tested in Paper I.

6.2. Other Cluster Candidates

We now consider those fields in which no overdensity associated with the radio source is found. In Table 3 we report for such fields the overdensities that would be associated with the radio galaxies if their photometric redshifts, as estimated in B13, had significantly higher photometric redshift errors. We adopt the same column description as in Table 2. We do not consider source number 31, for which a spectroscopic redshift is available. We also report only those overdensities that are still detected if a smaller redshift bin Δz is chosen throughout the PPM procedure. Interestingly, among these other overdensities, there is a high significance 3.5σ overdensity which is detected in the field of 13 at a redshift $z = 1.42 \pm 0.06$. Zatloukal et al. (2007) also found the presence of a cluster candidate (i.e., their cluster candidate number 13) in the same field at the redshift $z = 1.45$. We suggest that the two overdensities correspond in fact to the same cluster.

6.3. The Remaining Fields

We discuss in this section the remaining cases for which the difference between the redshift of the source and the redshift of any overdensity detected in the field is too large to make the association plausible. This is the case for sources 11, 30, 31, 70, 224, and 258.

Source 11 is an HLRG with a photometric redshift $z = 1.57^{+0.14}_{-0.09}$. No overdensity is found in its field within the redshift range $z_{centroid} = 0.4$–4.0 considered by the PPM.

Source 30 is an LLRG with a photometric redshift $z = 1.06^{+0.11}_{-0.07}$. Three overdensities are found in its fields. Their estimated redshifts are $z = 1.36$, 1.82, and 2.30, respectively. Their detection significances are 2.0σ, 2.0σ, 2.7σ.

Source 31 is an LLRG at $z_{\rm spec} = 0.91$. Four overdensities are detected in its field at redshifts $z = 0.70$, 1.91, 2.27, and 3.62, respectively. They are detected at a significance level of 3.6σ, 2.1σ, 3.1σ, and 2.7σ. Note that none of these overdensities would be associated with the radio galaxy if the photometric redshift $z = 0.88^{+0.03}_{-0.05}$ were adopted from B13, instead of the spectroscopic redshift. As outlined in Section 6.1, a group was found by previous work in the field of 31. The estimated redshift and mass are $z = 0.91$ and $M = 8.9 \times 10^{12}\ M_{\odot}$, respectively (Knobel et al. 2009). As discussed in Section 8 and tested in Paper I the PPM is more effective at finding richer groups and clusters. Therefore, it is not surprisingly that our method does not detect this relatively low mass group.

Source 70 is an HLRG with a photometric redshift $z = 2.32^{+0.53}_{-0.20}$. One single overdensity at $z = 0.49$ is detected in its field, with a significance of 2.0σ.

Source 224 is an LLRG with a photometric redshift $z = 1.10^{+0.10}_{-0.04}$. In Figure 9 (panel (d)), we report the corresponding PPM plot. Three overdensities are detected in its field at redshifts $z = 0.46$, 2.58, and 3.88, respectively. Their high significance patterns are in fact clearly visible in the PPM plot. Their significance levels are 2.3σ, 2.5σ, and 2.6σ.

Source 258 is an LLRG with at $z_{\rm spec} = 0.9009$. Four overdensities are detected in this field at redshifts $z = 2.07, 2.40$, 3.03, and 3.24, respectively. They are detected with significances of 3.4σ, 2.4σ, 2.5σ, and 2.3σ.

6.4. Multiple Associations

As is clear from Table 2, multiple associations are found in the case of sources 03, 25, and 28, only. As outlined in Paper I, multiple overdensities might be detected (1) in the presence of projection effects; (2) because of incorrect photometric redshift estimates that might be affected by systematics, especially in the case of the dimmer cluster members (e.g., those with AB magnitude $i^+ \sim 24$ in the I09 catalog); and (3) as a result of multiple local maxima that characterize the patterns of the PPM plot around a given redshift $z_{\rm centroid}$.

We here reconsider in detail all cases where we find multiple overdensities associated with a single galaxy. As mentioned above, two overdensities are associated with source 25 (see also Figure 9, panel (c)). They have similar significances ($\sim 2.5\sigma$) and they are also both detected starting from 50 arcsec from the location of the FR I. Such an angular separation corresponds to ~400 kpc at the redshift of the LLRG. Similar sizes of ~0.7–1.0 Mpc are estimated for the two overdensities (see Table 2).

We visually inspected the field of this source and we did not find any evidence that the non-null offset and the multiple association are present because of an artificiality or a technical bias of the I09 catalog occur at the redshift of the radio galaxy (e.g., that some sources at the redshift of the cluster candidate and in the field of the FR I are not included in the I09 catalog or that their redshifts are erroneously estimated). Since we do not find any clear discrepancy between the two overdensities and, furthermore, we estimate similar properties for these two megaparsec-scale structures, we suggest that both the detections are real and they could also correspond to a single cluster candidate associated with source 25.

As mentioned above, two $\sim 2.5\sigma$ overdensities are associated with HLRG 03 (see also Figure 9, panel (b)). They are both detected starting from the coordinates of the radio galaxy (i.e., $r_{\rm min} \sim 0$ arcsec) and their estimated sizes are similar (i.e., ~500–600 kpc; see Table 2). However, they are detected at significantly different redshifts $z = 1.82$ and 2.39, respectively. Analogously to the case of source 25, we visually inspected the field of 03 and we did not find any evidence that the multiple association is present because of a technical bias. Therefore, both overdensities are equally considered good, but distinct, cluster candidates, since they are found at different redshifts.

Two overdensities are associated with source 28. They are detected at similar (but different) redshifts $z = 2.71$ and 2.98, and with similar significances ($\sim 2.0\sigma$–2.5σ). We also estimate similar sizes for both of them (i.e., ~0.8–1.0 Mpc; see Table 2). However, we find that the overdensity at the lower redshift starts to be detected from 87 arcsec from the radio galaxy. This corresponds to ~700 kpc at the redshift of the overdensity. Analogously to the case of sources 03 and 25, we visually inspected the field of 28 and we did not find any evidence that the non-null offset and the multiple association are present because of a technical bias. Since we do not find any clear discrepancy between the two overdensities, but nevertheless we estimate different redshifts, we are not able to conclude if the associations correspond either to two separate megaparsec-scale overdensities at different redshifts or to a single megaparsec-scale structure that is identified as a double pattern in the PPM plot.

6.5. The Clean Catalog

We repeat all analyses not considering sources that are classified as stars, X-ray AGNs, or that are in masked areas in the I09 list. Hereinafter we refer to this as the clean catalog. Stars and X-ray AGNs are about ~4% of the sources in the catalog, while masked sources are about ~13%–18% (in the redshift range of our interest). The fields of 36 and 285 were almost completely masked-out most likely because the seeing in the Subaru optical images (Taniguchi et al. 2007) was poor. We visually inspect the *HST* image of these fields and we find that all masked-out objects are in fact galaxies. Therefore, in these cases we include these masked out objects in our analysis. If the full I09 catalog is adopted we find evidence of overdensities in both of these fields.

Interestingly, we find evidence for a 2.5σ overdense region associated with the radio galaxy 234 only if the clean catalog is adopted, while no overdensity is found if the complete I09 catalog is adopted. We visually inspect the *HST* image of that field and verify that some sources have been masked south of the location of source 234 because they are most likely foreground bright sources. We also find evidence for a segregation of $z \sim 0.93$ sources in the proximity of the radio galaxy 234. We believe that the discrepancy in adopting the two I09 catalogs is due to the fact that the estimated mean number density of the COSMOS field is lower if the clean catalog is adopted rather than if the full catalog is considered, while the number of masked sources in the field of 234 is low enough to detect the overdensity only if the clean catalog is used. For the sake of completeness, we report the overdensity associated with source 234 in Table 2. The fields of 36, 234, and 285 are the only cases for which we find a significant difference adopting the two I09 catalogs.

6.6. Inferred Cluster Size

In this section we limit our discussion to the cluster core sizes estimated by the PPM. The PPM detects all of the overdensities within given areas in the projected sky around the location of each radio galaxy. The procedure is fully described in Paper I and summarized in Section 5. The PPM infers the minimum and maximum distances from the coordinates of the radio galaxy at which the overdensity is detected.

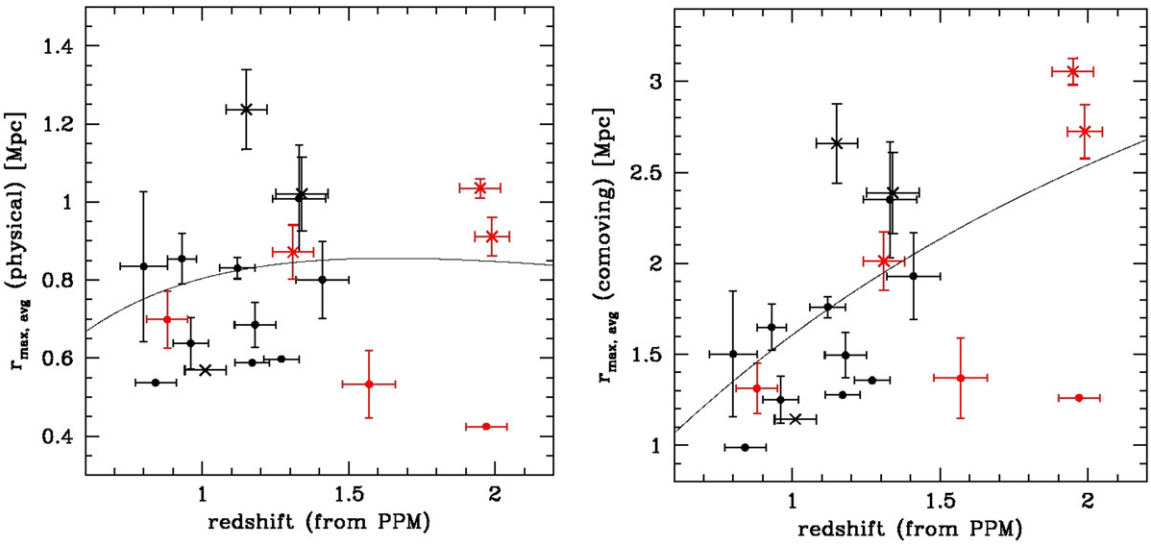

Figure 10. Cluster sizes estimated by the PPM as a function of their estimated redshifts. The reported uncertainties are the 1σ rms dispersions around the average. No error is reported in those cases where the rms is null. Cluster candidates around the HLRGs (red points) and the LLRGs (black points). Overdensities detected starting from a non-null angular separation from the locations of the radio galaxies are plotted as crosses. The remaining overdensities are plotted as full points. Sizes are plotted in physical units (left) and in comoving units (right). Sources with multiple overdensity detections have been conservatively rejected. The solid black line shows the physical (left panel) and comoving (right panel) sizes that correspond to 100 arcsec at each redshift.

(A color version of this figure is available in the online journal.)

The distances are estimated by averaging over all the points of the PPM plot having the significance of the overdensity and located around the redshift of the overdensity at the fixed bin ($\Delta z = 0.28$). Such estimates are shown in Table 2 for our cluster candidates. Both the average and median values are reported. The median values are less affected by the outliers and are always nevertheless consistent with the corresponding averages within the rms uncertainties. These aspects suggest that the overdensities are detected in the projected space with good accuracy and that these detections are stable with respect to a different choice of parameters (i.e., a different centroid of the redshift bin adopted).

In Figure 10 we plot the comoving (right panel) and physical (left panel) average maximum radii for each overdensity, along with the corresponding rms dispersions as a function of the estimated redshift of the overdensity along with its formal uncertainty. We conservatively reject all sources with multiple overdensity detections.

The cluster candidates around the LLRGs have, on average, comoving (physical) estimated sizes of $r_{\rm avg} = 1672(784)$ kpc, with an rms dispersion around the average of 522 (211) kpc and a median value $r_{\rm median} = 1501(800)$ kpc. The overdensities around the HLRGs have an estimated average comoving (physical) size of $r_{\rm avg} = 1955(745)$ kpc, an rms dispersion around the average of 780 (236) kpc, and a median value $r_{\rm median} = 2012(871)$ kpc. If we do not distinguish between the two different classes we have an average comoving (physical) value of $r_{\rm avg} = 1762(772)$ kpc, an rms dispersion around the average of 607 (213) kpc, and a median value $r_{\rm median} = 1501(800)$ kpc.

Note that these are only rough estimates of the core size of our cluster candidates. However, concerning our project, we can use them to infer interesting considerations (see also Sections 8.7 and 8.8). In general, these results suggest that the overdensities in our sample have similar core sizes, independently of the class considered (i.e., the LLRGs or the LHRGs).

More in general, there seems to be a trend where high-redshift sources are also found in overdensities with higher comoving sizes. We do not find any statistical significance by performing the Spearman test. Nevertheless, we cannot exclude that less dense overdensities occur at high redshifts. Diffuse protoclusters with star-forming galaxies have been in fact found at redshifts higher than $z \sim 2.0$ (Steidel et al. 2000; Venemans et al. 2007; Capak et al. 2011; Noble et al. 2013). However, we suspect that this trend is artificial and due to the dependence of the estimated size with redshift or by the low number count statistics. Another possibility is that the cluster size could be overestimated at most by a factor of $\sim$2 if (1) the radio galaxy were not located in the central regions of the cluster core (as tested in Paper I), and (2) in the cases when $r_{\rm min}$ is not null (the crosses in Figure 10), where $r_{\rm max}$ might not be a good cluster size estimator (see also discussion in Section 8.8).

6.7. The Minimum Distances

The cases where the minimum distances are estimated to be small or null likely correspond to those where the coordinates of the radio galaxy fairly coincide with the center of the associated overdensity.

However, some of the overdensities are detected starting from a positive angular separation of $\gtrsim$50 arcsec from the coordinates of the radio galaxy. Such an offset corresponds to a physical scale of 422 kpc at the median redshift estimated for our cluster candidates (i.e., $z = 1.3$).

These cases are controversial and are further discussed in Section 8.8. They might be megaparsec-scale overdensities where the radio galaxy is in the outskirts of the overdensity. This has been investigated in Paper I through the help of simulations. We have found that the method is able to detect cluster candidates even if the coordinates of the cluster are known with an accuracy of $\sim$100 arcsec and that the inferred minimum radii are only in some cases greater than zero. Alternatively, in these cases the radio galaxies might be hosted in underdense regions within their cluster environment.

As outlined above, we also visually inspected the fields of some sources (namely, 25 and 28) for which the overdensity

starts to be detected from a non-null separation from the location of radio galaxy. Even if we find a depletion in the number of photometric redshifts around the radio galaxy around its assumed redshift, we are confident that no technical bias occurred, concerning the estimation of photometric redshifts in the I09 catalog.

7. THE PAPOVICH METHOD

In this section we adopt a method (Papovich 2008, hereinafter P08) based on an IR color selection to search for cluster candidates in the field of the galaxies of our sample. The P08 method has been widely used in the literature (Mayo et al. 2012; Galametz et al. 2012; Wylezalek et al. 2013) to search for clusters at $z \gtrsim 1.3$; it utilizes the 1.6 μm bump in the SED of red galaxies, due to a minimum in the opacity of the H^- ion, present in the atmospheres of cool stars (John 1988; Galametz et al. 2012, and references therein). We apply such a method to our sample to see how many objects we can positively detect. In Section 7.1 we compare these results with those obtained by adopting our newly developed PPM.

The P08 method requires wide field observations at both 3.6 and 4.5 μm. We use the *Spitzer*-COSMOS (S-COSMOS) archive catalog.[12] S-COSMOS covers the entire COSMOS field. It is a deep infrared imaging survey carried out with the *Spitzer* Telescope. Megaparsec-scale overdensities are identified as regions of higher concentration of red sources with respect to the average density, which is derived as follows, similarly to what was done in previous works (Mayo et al. 2012; Galametz et al. 2012).

We choose ~300 randomly selected non-overlapping circular fields of 1 arcmin radius each. The number of the fields is limited and cannot be increased indefinitely because we require the fields to be non-overlapping and to lie within the COSMOS area.

We conservatively consider the objects in the S-COSMOS catalog that are detected at both 3.6 and 4.5 μm with a signal to noise ratio S/N > 10. This criterion is equivalent to that applied by P08 and similar to what was done in previous works (Galametz et al. 2012; Wylezalek et al. 2013). The S/N limit ensures that only well-detected objects enter the sample (Papovich 2008). We also limit our analysis to those sources that are brighter than 1 μJy, which is the confusion limit of the S-COSMOS survey at both 3.6 and 4.5 μm (Sanders et al. 2007).

Then, we select all sources satisfying $([3.6] - [4.5])_{AB} > -0.1$ mag. Hereafter we denote with [3.6] and [4.5] the apparent AB magnitudes at the (observer frame) wavelength equal to 3.6 and 4.5 μm, respectively.

In Figure 11 we plot the number count distribution for the ~300 fields as a function of the number of sources in each field that satisfy the P08 criterion.

Similarly to what was done in Mayo et al. (2012) and Galametz et al. (2012), we fit such a distribution with a Gaussian function, iteratively clipping at 2σ above the best fit average. This is done in order to exclude from the fit the high number count tail of the distribution. In fact, it might be contaminated by those fields that are populated by a significantly high number of red objects. They might be associated with megaparsec-scale overdensities and therefore, not representative of the overall number count distribution in the COSMOS survey.

We estimate the average number of sources per field which satisfy the P08 criterion. It is equal to $N = 30.0 \pm 6.4$ where the average and the reported uncertainty are the mean value and square root of the variance of the best fit Gaussian function, respectively.

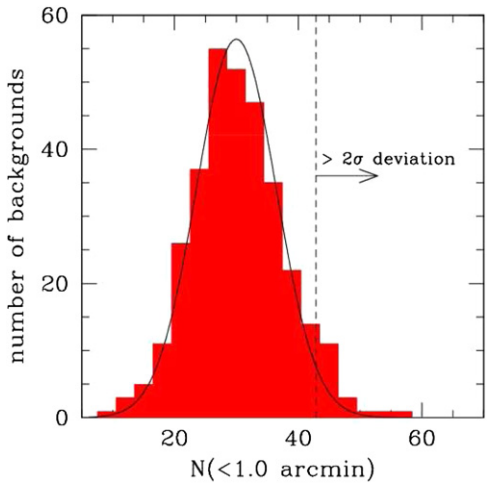

Figure 11. Results of the Papovich (2008) method. Red histogram: distribution of sources within ~300 randomly selected non-overlapping circular fields of 1 arcmin radius selected from the COSMOS area. The solid line represents the Gaussian best fit curve obtained by iteratively clipping at 2σ above the best fit average. The vertical dashed line is located at the 2σ deviation from the best fit average.

(A color version of this figure is available in the online journal.)

For each 1 arcmin radius field centered around the galaxies in our sample we count the sources in the S-COSMOS catalog that satisfy the P08 criterion, analogously to what was done for each of the ~300 randomly selected fields. Then, we estimate the overdensity significance level as the ratio of the number excess with respect the average $N = 30.0$ and the 1σ dispersion ($= 6.4$) associated with N.

The P08 method is expected to be effective at redshifts $z \gtrsim 1.3$ (see, e.g., Galametz et al. 2012; Mayo et al. 2012). As discussed further in Galametz et al. (2012), this is due to the fact that the specific color selection criterion detects the rest-frame 1.6 μm bump in the SED of the galaxies, which originates from a minimum in the opacity of the H^- ion in the atmospheres of cool stars (John 1988). Such a feature is redshifted out of the *Spitzer* filters at 3.6 μm and 4.5 μm, in the case of lower redshift ($z \lesssim 1.3$) sources.

Note that, even if the radio galaxy is at a redshift $z < 1.3$, the P08 method might detect those overdensities in the field that are not associated with the radio galaxy, but are at $z \geqslant 1.3$. As discussed in Section 6.2 and as is clear from visual inspection of the PPM plots in Figure 9, overdensities not associated with the radio galaxy are also found by the PPM in the fields of the radio sources, at different redshifts.

The results of the P08 method are shown in Table 4, where we report the number counts and the associated significance levels of the overdensities in the fields of the sources in our sample. In the table we only report two objects at $z < 1.3$, namely, 13 and 39. This is because these are the only two fields at $z < 1.3$ in which overdensities are detected by such a method. For all other objects that are not reported in the table the P08 method does not find any overdensity.

Negative significances correspond to underdense fields. Similarly to what was done in Galametz et al. (2012) and Mayo et al. (2012), we consider as dense megaparsec-scale environments only the regions with an overdensity detected at a level $>2\sigma$, i.e., sources with more than 42 counts within a 1 arcmin radius.

[12] http://irsa.ipac.caltech.edu/data/SPITZER/S-COSMOS/

Table 4
Papovich (2008) Method Results

ID	No. of Sources	σ	ID	No. of Sources	σ
02	36	0.93	32	33	0.47
03	51	3.26	34	31	0.16
04	47	2.64	37	38	1.24
05	28	−0.31	38	37	1.09
11	24	−0.93	39*	47	2.64
13*	49	2.95	70	33	0.47
22	40	1.56	202	34	0.62
25	30	0.00	226	34	0.62
28	47	2.64	228	33	0.47
29	49	2.95			

Notes. Column description: (1) ID number of the radio galaxy; radio galaxies 13 and 39 have photometric redshift $z < 1.3$ and are marked with an asterisk; (2) number of sources within 1 arcmin radius with flux >1 μJy and S/N > 10 at both 3.6 and 4.5 μm, as well ($[3.6]-[4.5])_{AB} > -0.1$ mag; (3) overdensity significance (in units of σ). Negative values refer to underdense regions.

According to the P08 method, six sources are found to be in a $\geqslant 2\sigma$ dense megaparsec-scale environment. The source for which the highest significance is observed is object 03 with a photometric redshift of 2.2. Note also that the field of 28, which has a photometric redshift $z = 2.9$, is detected with a $\sim 2.6\sigma$ significance. While this object is formally beyond the redshift range for which this sample has been built it is still an interesting case worth mentioning. This is because such an overdensity might be a $z \sim 3$ (proto-)cluster around a ∼2 orders of magnitude lower power radio galaxy than those commonly found in clusters or protoclusters at similar redshifts (Miley & De Breuck 2008; Galametz et al. 2013).

In the following sections we discuss the results obtained by the P08 method and we compare them with those of the PPM.

7.1. Comparison with the Results of the Papovich (2008) Method

We compare our results with those obtained independently by using the P08 method, as described in Section 7. All six cluster candidates found with the P08 method are also detected by the PPM. Five of them are associated with radio galaxies in the sample, according to the PPM procedure. The sixth overdensity is the cluster candidate found in the field of 13 by both the PPM and the P08 method. However, according to the method, such an overdensity is not associated with the radio galaxy by the PPM (see Section 6.2). Note that all of the six overdensities detected by both the P08 method and the PPM are at redshift $z \gtrsim 1.3$ (within the corresponding uncertainties), as estimated by the PPM procedure. This is also true for the overdensities in the fields of 13 and 39. Even if the radio sources are at redshifts $z = 1.19\pm^{0.08}_{0.11}$ and $z = 1.10\pm^{0.05}_{0.05}$, the PPM detects overdensities in their fields at $z = 1.42 \pm 0.06$ and $z = 1.27 \pm 0.06$, respectively. These results are not surprising since the P08 method is effective at finding clusters at $z > 1.3$.

Excluding the overdensity in the field of 13 that is not associated with source 13, only 5 out of the 12 cluster candidates at $z \gtrsim 1.3$ in our catalog are also found with the P08 method. Among the 12 clusters we conservatively do not consider the overdensities in the fields of sources 38 and 228. Even if these sources have photometric redshifts $z = 1.30\pm^{0.17}_{0.28}$ and $z = 1.31\pm^{0.05}_{0.07}$, respectively, the PPM detects clusters in their fields at redshifts below $z = 1.3$.

Two out of the five clusters, namely, 29 and 39, that are associated with the radio galaxies and detected by both the P08 method and the PPM, are around LLRGs, the other three (namely, source 03, 04, and 28) are around HLRGs. As discussed above, source 39 is the only source out of those five that has a photometric redshift below $z = 1.3$.

If we consider our seven cluster candidates at $z \gtrsim 1.3$ in our catalog that are not detected by the P08 method we find that three of them are associated with LLRGs (i.e., sources 2, 22, and 25). The remaining four out of the seven are associated with $z \gtrsim 1.3$ HLRGs (i.e., 05, 34, 37, and 226). Since the P08 method was primarily designed to search megaparsec-scale overdensities at these redshifts, it is interesting that many of our $z \gtrsim 1.3$ cluster candidates are not detected by such a method. It is therefore worth reconsidering in more detail our cluster candidates found around our $z \gtrsim 1.3$ sources.

Three of our cluster candidates are at $z \simeq 2$. These are the overdensities associated with sources 03, 05, and 226. As mentioned before, the presence of megaparsec-scale overdensities around those sources were previously suggested in C10. Interestingly, the P08 method finds the overdensity in the field of 03 only.

If we focus on the nine $1.3 \lesssim z \lesssim 2$ sources that the PPM finds to be in dense megaparsec-scale environments, (i.e., sources 02, 04, 22, 25, 29, 34, 37, 38 and 228) we find that only two out of the nine are found in dense environments by the P08 method (i.e., sources 04 and 29). However, among them, the estimated redshifts of the cluster candidates associated with sources 37 and 38 are only marginally consistent within the redshift uncertainties of the two sources. These two cases could correspond to false positive overdensity PPM detections. Furthermore, the P08 method should not be able to detect the $z = 0.88$ overdensity associated with source 38, since such a redshift is well below the redshift range where the method is effective. The case of 37 is different; this is because the overdensity associated with this source has an estimated redshift $z = 1.95$. Therefore it falls within the redshift range allowed by the method.

Excluding source 38, the results reported above imply that $75\% \pm 15\%$ of our $1.3 \lesssim z \lesssim 2$ cluster candidates are not detected by the P08 method (we have conservatively excluded the above mentioned source 39 that is at a redshift formally below $z = 1.3$). Such a percentage decreases down to to $71\% \pm 17\%$ if source 37 is also not considered.

We consider separately the high-redshift $z \sim 3$ source 28 that is detected to be in a dense environment at $\sim 2.6\sigma$ and $\sim 2.5\sigma$ significance levels by the P08 method and by the PPM method, respectively. Even if such a redshift is formally beyond the redshift interval ($z \sim 1$–2) of our interest, we do not reject the source.

These results suggest that the great majority ($\gtrsim 70\%$) of our $z \gtrsim 1.3$ cluster candidates are not detected by the P08 method, while all the seven cluster candidates found with such a method are also detected by the PPM. This suggests that our method might be more effective at finding cluster candidates, at least limited to our sample and data set used. We will further discuss these results in the following section.

7.2. Do We Find Blue or Still Forming Clusters?

In the previous section we found that the great majority (i.e., ∼70%) of our $z \gtrsim 1.3$ cluster candidates are not detected with the P08 method, while all of the cluster candidates detected by such a method are also found with the PPM. This is interesting, since such redshifts correspond to the range within which the P08 method is effective (Galametz et al. 2012). Although we

cannot fully understand the details for such a discrepancy we believe that the method might miss those overdensities that do not fulfill the specific P08 color selection.

This result could also have physical implications. The P08 method searches for segregations of red $([3.6]-[4.5])_{AB}$ galaxies. In principle, it is sensitive to both passively evolving and star-forming galaxies. However, the method might miss overdensities that are populated by a great amount of bluer galaxies than those required in order to detect the overdensity.

As argued by Muzzin et al. (2013), foreground galaxies at redshift $0.2 < z < 0.4$ have colors similar to those at redshift $z > 1.0$ and might add noise, thus affecting the detections.

Furthermore, we also found that the majority of the objects that are used for the PPM and are selected within the I09 catalog are not included in the S-COSMOS survey and, therefore, they are not used by the P08 method. Hence, a mismatch between the P08 method and the PPM is not surprising.

Note that we applied the P08 method by performing a counts-in-cell analysis, i.e., we counted objects within a fixed circle centered at a given position in the sky, as done in previous work (e.g., Galametz et al. 2012; Mayo et al. 2012; Wylezalek et al. 2013).

On the contrary, the search for cluster candidates performed in this work by adopting the PPM is based on number counts and does not rely on peculiar and specific properties (e.g., colors of the sources) and a specific segregation of the galaxies within the cluster core (see also Section 8.8).

Since the P08 method is applied performing a counts-in-cell analysis, some of the clusters that are not detected by such a method might be populated by galaxies that are not completely segregated in the cluster core.

Interestingly, C10 suggested the presence of a high fraction of star forming galaxies in the $z \sim 2$ cluster candidates associated with sources 03, 05, and 226, on the basis of the visual inspection of the RGB images of their fields.

In a forthcoming paper we will analyze the color magnitude diagrams to study the star formation activity of the galaxies in our clusters and address the problems of detecting and studying the red sequence, as well as understanding where star forming and quiescent galaxies are located within the cluster.

The evidence for star formation activity in some of our clusters is not surprising, especially at $z \gtrsim 1.5$, where cluster galaxies are expected to have ongoing or increasing star formation (Zeimann et al. 2012). In fact, in some of these high-redshift clusters, a significant fraction of the cluster galaxy population is constituted by highly dust reddened sources (Strazzullo et al. 2013) or by blue and irregular galaxies (Tozzi et al. 2013).

From a theoretical point of view, previous studies made predictions for the mass function of galaxy clusters (e.g., Bode et al. 2001; Tinker et al. 2008). However, since the cluster/group population at redshift $z \gtrsim 1.5$ is limited to a few known spectroscopically confirmed clusters, observational studies are limited to single high-redshift clusters. This implies that the mass function is only poorly determined by observations.

The spectroscopic confirmation of our $z \gtrsim 1.5$ cluster candidates would increase the number count statistics. This will help in constraining the cluster mass function and will support previous cluster studies from both a theoretical and observational point of view.

8. DISCUSSION

The main goal of this project is to confirm that FR I radio galaxies at redshifts $z \sim 1$–2 are preferentially found in rich groups or clusters, as already proved for local objects, at variance with that found for local powerful FR II sources (Hill & Lilly 1991; Zirbel 1997; Wing & Blanton 2011). For this reason we selected a subsample of bona fide LLRGs from the original C09 sample. This was done to derive a sample of sources with radio powers compatible with those of FR Is at low redshifts.

We also examine the properties of the subsample of relatively high radio power objects (HLRGs) with respect to the LLRGs. In the following we discuss the implications of our results for these two groups of objects.

8.1. Megaparsec-scale Environments of the C09 Sample

As reported in Section 6 both LLRGs and HLRGs are found in dense environments. The fraction of galaxies in groups or clusters is about ∼70% for both subsamples, consistent within the 1σ uncertainties. We also found that the detected overdensities have comparable (within a factor of ∼2–3) estimated sizes, independent of both the subsample and the redshift considered (we will discuss this in detail in Section 8.7). Therefore, a posteriori, this result strongly suggests that, on a statistical basis, the two subsamples constitute a single population of radio galaxies with similar megaparsec-scale environments and similar properties.

8.2. Comparison with Low-redshift Radio Galaxy Environments

We found that the majority (69%±8%) of the radio galaxies in our sample reside in dense environments. Here we quantitatively compare our results with the results obtained for samples of low redshift FR Is.

Note that it is difficult to compare the estimated cluster richness of our candidates with that of other samples of low redshift clusters associated with radio galaxies. This is mainly because of the different data sets used and of the different techniques employed in measuring the cluster richness.

Zirbel (1997) found that 70% (with an estimated uncertainty of 11%)[13] of low redshift (i.e., $z < 0.25$) FR Is in their sample reside in intermediate or rich groups (i.e., structures with 10 or more members). In terms of richness, these groups could roughly correspond to the overdensities detected by the PPM around the radio galaxies in our sample.

Instead, only (24 ± 8)% of the low redshift (i.e., $z < 0.25$) FR IIs in the Zirbel (1997) sample reside in intermediate or rich groups. Such a percentage increases up to (41 ± 8)% if high-redshift (i.e., $0.25 \lesssim z \lesssim 0.5$) FR IIs are considered. The results obtained by Zirbel (1997) are also in agreement with that independently found for FR IIs at $z < 0.3$ by Smith & Heckman (1990) and that found by Ramos Almeida et al. (2013) for a $z \leqslant 0.7$ sample of luminous radio galaxies, mainly comprised of FR IIs.

Interestingly, the fraction we found for the $z \gtrsim 1$ sources in our sample is fully consistent with the percentage (i.e., 70%) found by Zirbel (1997) for their sample of low redshift (i.e., $z < 0.25$) FR Is. Note that this holds not only for the LLRGs but also for the HLRGs. This implies that the environments of FR Is and FR IIs are different and that they also evolve differently with redshift. While the majority of FR Is seem to be found in rich groups or clusters at all redshifts, the FR IIs seem to inhabit rich environments only at $z > 0.25$. However, as discussed in the following section, the fraction of FR IIs that reside in rich

[13] We estimated the error on the percentage by adopting 1σ uncertainties according to the binomial statistics, for consistency with our results.

groups or clusters is significantly lower than that of FR Is even at higher redshifts.

8.3. Comparison with High-z FR IIs

In this section we compare our results with the environment properties found for high-redshift FR IIs. Note that, thanks to the analysis of the C09 sample, this is the first time that the environments of FR Is and FR IIs can be directly compared at such high redshifts.

High-redshift ($z \sim 1$–2), low-power radio galaxies (i.e., FR Is) are found in rich environments more frequently than high-power FR IIs at similar redshifts. In fact, if we consider the sample of high-redshift ($z \gtrsim 1.3$) powerful FR IIs studied by Galametz et al. (2012), 11 out of 48 objects (i.e., $23\% \pm 7\%$) reside in megaparsec-scale environments that are at least 2σ denser than the field.

However, Wylezalek et al. (2013) extended this analysis to a larger sample of 387 radio galaxies at $1.3 < z < 3.2$. They found evidence for dense environments for 55% of these sources. Interestingly, this percentage is consistent with that found for FR II radio galaxies at redshifts $z \sim 0.5$ ($\sim$50%; Hill & Lilly 1991).

Note that the radio powers that characterize the objects in all of the samples cited above ($L_{1.4} \gtrsim 10^{34}\,\mathrm{erg\,s^{-1}\,Hz^{-1}}$) are about two order of magnitudes higher than those of all of the radio galaxies in our sample, including the HLRGs. Hence, they undoubtedly represent a different class of radio galaxies.

The comparison between our results and those cited above for powerful high-z FR IIs confirms that the environment of high-redshift FR Is and FR IIs is different.

This implies that the megaparsec-scale environments of FR Is and FR IIs undergo a different evolution. If we adopt a $\sim$50% level of FR IIs in clusters at high redshifts as a fiducial value, we could conclude that at $z > 0.5$ the environments of FR Is and FRII s are similar (but not identical!). However, as we already discussed above, this is clearly not true at lower redshifts. Furthermore, the values reported in Galametz et al. (2012) and Wylezalek et al. (2013) are not consistent with each other within the number count uncertainties. Wylezalek et al. (2013) suggested that this may be due to the small size of the Galametz et al. (2012) sample. It might be interesting to study in more detail the selection criteria of these two samples in order to test whether the differences are due to significant discrepancies in the two sample selections.

Therefore, in light of the results presented here, we confirm that the connection between the active nucleus and its large-scale environment could play a fundamental role in determining the specific properties of each radio galaxy. Clearly, it would be interesting to study X-ray or optically selected samples of clusters of galaxies at redshifts $z \gtrsim 1$ to investigate how the cluster properties (e.g., richness, halo mass, gas content, and X-ray luminosities) are related to those of the hosted radio galaxies (e.g., their radio power, their number within the cluster sample, and the mass and size of the host galaxy) and more in general, to those of the entire cluster galaxy population. However, these studies require complete and well studied samples of clusters. Therefore, previous work has been so far limited to low or intermediate redshifts (e.g., Ledlow & Owen 1996).

8.4. Intermediate Redshift Cluster Samples

We here focus on previous studies on intermediate ($0.3 \lesssim z \lesssim 1$) redshift cluster samples. Radio sources with radio power $L_{1.4} \simeq 10^{32-33}\,\mathrm{erg\,s^{-1}\,Hz^{-1}}$ which is typical of those of the objects in our sample, are found in 10%–20% of the X-ray and optically selected clusters (Branchesi et al. 2006; Gralla et al. 2011).

However, such a percentage rapidly increases up to $\gtrsim$90% if lower power radio sources are included ($L_{1.4} \simeq 10^{30}\,\mathrm{erg\,s^{-1}\,Hz^{-1}}$; Branchesi et al. 2006). This is in agreement with previous studies on local Abell clusters (Ledlow & Owen 1995, 1996).

The fact that such a fraction increases for low-power sources might be explained as a straightforward consequence of the steepness of the radio luminosity function of the radio galaxies in clusters (Branchesi et al. 2006). This strongly confirms that low-power radio galaxies can be more successfully used to search for clusters of galaxies than radio galaxies with higher power.

8.5. Detection Efficiency

The number density per unit redshift ($dn/dz/d\Omega$) in the COSMOS survey is low and it is equal to $\simeq$25, 10, and 3 arcmin^{-2} at redshifts $z \simeq 1$, 1.5, and 2.0, respectively (Ilbert et al. 2009). The steep decrease of the number counts for increasing redshifts is a strong constraint for all of the methods (including the PPM) that search for megaparsec-scale overdensities on the basis of number counts (Scoville et al. 2013).

In addition, photometric and spectroscopic redshifts cannot be easily obtained within $z \sim 1$–2, where most of the relevant spectral features fall outside of the instrumental wavelength bands (Steidel et al. 2004; Banerji et al. 2011).

Therefore, methods that are based on number counts and redshift information and that are used to search for clusters and groups in the COSMOS survey are usually applied up to redshifts $z \lesssim 1$ (e.g., Knobel et al. 2009; George et al. 2011; Knobel et al. 2012), or at redshifts higher than $z \simeq 2$ (e.g., Diener et al. 2013). Note also that such methods commonly use spectroscopic redshifts so that a small number (i.e., $\lesssim$5) of cluster galaxies is sufficient to establish the presence of a cluster or group candidate.

The clusters in our sample are detected within the entire redshift range $z \sim 1$–2 of our interest. For each overdensity we estimate detection significance, redshift, and size. The overdensities are detected up to 5.6σ significance. All these results are ultimately due to the flexibility of the PPM to obtain robust results in presence of low number counts. The overdensities are detected with median significances of 3.3σ and 2.5σ for the LLRGs and the HLRGs, respectively. Since the cluster candidates around the LLRGs and the HLRGs have a median redshift $z = 1.17$ and $z = 1.97$, respectively, we suggest that the discrepancy between the detection significances of the clusters associated with the two different subsamples is due to the decreasing number counts in the COSMOS survey for increasing redshifts. However, such discrepancy is relatively small considering that the number density in the COSMOS field dramatically drops down by a factor of $\sim$8 from $z = 1$ to $z = 2$ (Ilbert et al. 2009).

In Paper I we tested the ability of the PPM to detect overdensities at different redshifts, with richness and size spanned within the ranges found for the cluster candidates in our sample. Interestingly, we found that our method is able to efficiently detect clusters within our redshift interval, despite the wide range allowed for the cluster richness and size.

Therefore, we are confident that the detection efficiency (i.e., the number of clusters with homogeneous properties that

are potentially detectable per unit redshift by the PPM) is fairly constant with redshift. The fact that the detection rate is about 70% for both our subsamples confirms it a posteriori. Conversely, if the detection efficiency dramatically decreased for increasing redshifts, we would significantly underestimate the fraction of HLRGs in clusters.

8.6. The $z \gtrsim 1.5$ Cluster Candidates

Six overdensities in our sample are found at redshift $z > 1.5$. These correspond to sources 03, 04, 05, 28, 37, and 226. All of them are HLRGs. The fact that we find six overdensities at such a high redshift, despite the small area of the COSMOS survey, further suggests that these might be clusters with a low or intermediate mass (i.e., $M \simeq 10^{13-14}\ M_{\odot}$).

Furthermore, the number density of clusters of higher mass (i.e., $M \gtrsim 10^{14}\ M_{\odot}$) is expected to drop down by more than an order of magnitude between $z = 1$ and $z = 2$, according to the current ΛCDM scenario (e.g., Bode et al. 2001; Tinker et al. 2008). In fact, clusters with masses $M \gtrsim 10^{14}\ M_{\odot}$, at redshift $z \sim 2$, are most likely the progenitors of massive $M \gtrsim 10^{15}\ M_{\odot}$ clusters at $z = 0$ (Chiang et al. 2013). Conversely, assuming hierarchical clustering (Cooray & Sheth 2002), at $z \sim 2$, groups of lower mass could represent a larger fraction of the group/cluster population than at lower redshifts.

Furthermore, by definition, groups have a lower richness than clusters, they exhibit fainter X-ray emission, and they have lower mass content in terms both of dark matter and gas than clusters of galaxies. They are therefore more difficult to find with the conventional techniques adopted for clusters. High-redshift groups are in fact usually identified up to $z \lesssim 1$ with methods such as those based on number counts (Knobel et al. 2012; More et al. 2012), or searching for strong lensing signatures originating from megaparsec-scale dark matter halos (Cabanac et al. 2007; Limousin et al. 2009; More et al. 2012, see also Section 8.9). Interestingly, if our cluster candidates were confirmed to be rich groups (see Section 8.7.1), they would constitute a high-redshift sample.

Diener et al. (2013) obtained a number of 42 candidate groups at $z \gtrsim 2$ in the COSMOS field. They used spectroscopic redshifts, so that a small number (i.e., $\lesssim$5) of members is effective at establishing the detection of a cluster candidate. Impressively, for the only object in common with our list (i.e., their cluster candidate 22 corresponds to our cluster candidate 03) the redshift and the size of the cluster estimated by the PPM fully agree with the spectroscopic measurement and the cluster size estimated in Diener et al. (2013).[14] Note that this cluster candidate was suggested by previous work (Chiaberge et al. 2010). With its five spectroscopically selected cluster members, this is the richest among the groups in the Diener et al. (2013) catalog.

On the basis of the redshift information, the authors also estimated the velocity dispersion of the cluster members (526 km s^{-1}) which is significantly higher than the average ∼300 km s^{-1} among the group candidates in their sample. This might suggest that the cluster members are still encompassing a spatial segregation and that the cluster is still forming, as also discussed for other cluster candidates in our sample (see also Section 7.2).

[14] The redshift and the size estimated by the PPM for one of the two overdensities associated with source 03 are $z = 2.39 \pm 0.09$ and 617 ± 57 kpc, respectively. Diener et al. (2013) found a spectroscopic redshift $z = 2.440$ and estimated a size of 412 kpc for their group candidate 22.

8.7. Cluster Properties

The general relationship among richness, size of the cluster, and the cluster mass is quite complex (i.e., it depends on the depth of the photometric catalog, the redshifts, the evolution of the luminosity function), especially at the redshifts of our interest ($z \sim$ 1–2), where the properties of the cluster galaxy population in terms of luminosity and segregation within the cluster are expected to evolve and are not fully understood. In the following sections we discuss size, mass, and richness estimates for the clusters we find in COSMOS.

8.7.1. Size and Mass Estimates for the $z \sim 1$ Clusters

In this section we compare our size estimates with those obtained by previous work for our $z \sim 1$ cluster candidates that are also found in the Finoguenov et al. (2007), Knobel et al. (2009), Knobel et al. (2012), and George et al. (2011) catalogs, namely, the clusters in the fields of 01, 16, 18, and 20. Interestingly, all of the cluster mass estimates in these catalogs are consistent with each other and the reported cluster sizes are in good agreement with ours.

In particular, for the cluster candidate associated with our source 01 we roughly estimate a core size of ∼71 arcsec (i.e., ∼500 kpc). On the basis of *Newton-XMM* data, Finoguenov et al. (2007) estimated the virial core mass and the size for the same cluster candidate. They reported $r_{500} = 48$ arcsec and $M_{500} = 5.65 \times 10^{13} M_{\odot}$ (see Table 1 in Finoguenov et al. 2007, for further properties).[15]

By assuming spherical symmetry and a β-model density profile for the cluster matter distribution (Cavaliere & Fusco-Fermiano 1978) we estimate r_{200} =76 arcsec.[16] George et al. (2011) estimated for the same cluster candidate a core size r_{200} = 73 arcsec, and a core mass $M_{200} = 5.25 \times 10^{13} M_{\odot}$, on the basis of the mass versus X-ray luminosity relation given in Leauthaud et al. (2010). Note that the George et al. (2011) group catalog was obtained by using photometric redshifts and previous X-ray-selected group catalogs. Both the Knobel et al. (2009, 2012) group catalogs were instead obtained by using spectroscopic redshifts. They reported fiducial mass estimates ($M \sim$ 6–9 $\times 10^{13} M_{\odot}$) for the megaparsec-scale overdensity associated with source 01. They were obtained by using spectroscopic redshift information. Knobel et al. (2012) also estimated a size of 659 kpc for this cluster candidate.

Concerning the cluster candidates in the fields of 16, 18, and 20, Knobel et al. (2009, 2012) reported masses $M \simeq$ 1.4–2.2 $\times 10^{13} M_{\odot}$ and sizes ∼327–378 kpc (Knobel et al. 2012). These sizes are roughly consistent even if lower than those estimated by the PPM for these three groups (∼600–800 kpc).

These results suggest that the $z \sim 1$ cluster candidates associated with sources 01, 16, 18, and 20 are all groups of intermediate/small size, even if that in the field of 01 is likely more massive than the others. (see also Section 8.9 for further discussion). Interestingly, this result seems to be independent of the cluster selection (i.e., optical or based on X-ray data). This is also consistent with previous work by Bahcall et al. (2003, see their Table 1), who found that the clustering lengths for optically selected clusters are comparable with (even if preferentially smaller than) those obtained for X-ray-selected clusters.

[15] Here r_{500} (r_{200}) is the radius encompassing the matter density 500 (200) times the critical one and M_{500} (M_{200}) is the mass enclosed within such radius.
[16] In estimating r_{200} we also assume hydrostatic equilibrium. We use Equation (3) of Reiprich & Böhringer (1999) and the core radius estimates as in Equation (4) of Finoguenov et al. (2007).

We nevertheless note that our cluster sizes are only rough estimates or upper limits of the cluster core in the optical bands (see also Section 6.6) and, therefore, a robust comparison with previous X-ray cluster sizes is beyond the purposes of our work. In particular, the core size might be overestimated by at most a factor of ∼2 if the radio galaxy is located in the outskirts of the cluster. This possibility is further discussed and tested in Paper I. Despite this, our estimates are reasonable and typical of rich groups and clusters for all of the clusters candidates in our sample. Furthermore, the sizes estimated in this work for each of the two subsamples (i.e., the LLRGs and the HLRGs) are consistent with each other within the uncertainties. On average, comoving and physical sizes for the cluster candidates in our sample are about 1.8 and 0.8 Mpc, respectively. Therefore, all these results allow us to draw general considerations on our cluster candidates, as shown in the following sections.

8.7.2. Cluster Richness and Mass

According to the PPM procedure, we count the galaxies within a redshift bin $\Delta z = 0.28$ centered at the estimated redshift of the cluster and within the projected area enclosed between the median values of angular separations $r_{\rm min}$ and $r_{\rm max}$ from the coordinates of the radio galaxy (see Table 2). This is not the number of cluster members, but simply the number of sources in the I09 catalog that are found in the field of each overdensity, around the estimated redshift of the cluster. Such a number can be considered as a rough estimate of the richness of the cluster because of both the instrumental and PPM limitations.

In detail, the overdensities in the fields of 18 and 26 are those that have the highest number of fiducial cluster members (i.e., ∼200). They are also detected at high significances (5.6σ and 3.9σ, respectively). About 100 galaxies are instead associated with the overdensities in the fields of 01, 02, 16, and 20, which are detected at significances of 3.5σ, 4.3σ, 3.5σ, and 3.9σ, respectively. About 50 sources are selected as cluster members of the overdensities associated with sources 39 and 228, which are detected at lower significance levels of 3.5σ and 3.2σ, respectively. At the high-redshift end of our sample (i.e., $z \simeq 2$) the overdensities are instead defined by only ∼10 galaxies, as it is, e.g., for sources 03 and 05, which are detected at 2.6σ and 2.2σ, respectively.

Therefore, the estimated number of the fiducial cluster members varies with the cluster detection significance from ∼10 for our cluster candidates at the highest redshifts ($z \sim 2$) to more than ∼200 for our $z \sim 1$ clusters candidates. This is most likely because of the overall decrease in the number count density of the COSMOS survey for increasing redshifts.

High-z faint cluster galaxies (i.e., $I \geqslant 25$) are not included in the I09 catalog and therefore we might miss a significant part of the cluster galaxy population. However, as discussed in Section 8.5, this does not affect much the detection efficiency of the PPM.

Also note that our method is not highly biased toward large-scale structures with specific characteristics. Previous work found that there is no clear correlation between cluster richness and mass and the radio power of the source up to intermediate redshifts ($z \lesssim 0.95$) for radio galaxies with radio power $L_{1.4} \simeq 10^{32}$ erg s^{-1} Hz^{-1} or even lower (Ledlow & Owen 1995; Gralla et al. 2011). However, Magliocchetti & Brüggen (2007) found contrasting results based on a small sample of 12 X-ray-selected clusters at low-intermediate redshift ($z < 0.3$). In particular, they suggested that low-power radio sources (down to $L_{1.4} \simeq 10^{28}$ erg s^{-1} Hz^{-1}) are preferentially hosted by low-mass clusters.

However, irrespective of the number of the fiducial cluster members estimated by the PPM, we expect that, on average, our group/cluster candidates have low or intermediate mass (i.e., $M \simeq 10^{13-14}\,M_{\odot}$). The fact that our size estimates are consistent with those found in previous work and are typical of those of rich groups and clusters strengthens such a scenario. Furthermore, as pointed out in Paper I, we stress that the PPM effectively finds systems whose masses are typical of rich groups, i.e., are below the typical cluster mass cutoff $\sim 1 \times 10^{14}\,M_{\odot}$. In particular, this is the case with our $z \sim 1$ cluster candidates that are found in previous catalogs of groups in the COSMOS field (see Section 6.6). This is clearly due to the small area of the COSMOS survey and the steepness of cluster mass function more than any detection biases of our method. Hence, we will extend our work to wider surveys (e.g., stripe 82 of the Sloan Digital Sky Survey (SDSS)), where we expect to have a higher chance of finding more massive structures.

8.8. The Location of the FR I within the Cluster

Previous work investigated the position of BCGs and radio galaxies in clusters. Ledlow & Owen (1995) found that about 90% of the radio galaxies hosted in local ($z < 0.09$) Abell clusters are located within 200 kpc from the cluster center. Furthermore, the great majority of such local radio galaxies are FR Is. Similarly, Smolčić et al. (2011) studied a sample of X-ray-selected groups up to $z \simeq 1.3$. They found that low-power radio galaxies ($L_{1.4} \simeq 10^{30.6-32.0}$ erg s^{-1} Hz^{-1}) are preferentially found within $0.2 \times r_{200}$ from the group center (i.e., about $\lesssim$60 kpc).

This could also be true at our redshifts. In fact, for the six cluster candidates that are found by other authors in the fields and at the redshifts of our sources (namely, 01, 03, 16, 18, 20, and 31) using different techniques (i.e., X-ray emission and overdensities based on redshift information, Finoguenov et al. 2007; Knobel et al. 2009; George et al. 2011; Knobel et al. 2012; Diener et al. 2013) we can compare the locations of our FR I beacons with the coordinates of the cluster centers, as estimated by these authors. We find that in the cases of 01, 03 and 31 the offset is less than ∼14 arcsec. They correspond to $\lesssim$120 kpc at the redshifts of the overdensities. In the cases of sources 16, 18, and 20 the association between our FR I beacons and the cluster candidates found in other catalogs (Knobel et al. 2009, 2012) is less certain. This is because the offset is higher than the cases outlined above. It is about 40 arcsec for sources 18 and 20 (i.e., ∼300 kpc at their redshifts) and it is ∼1 arcmin (i.e., ∼500 kpc) for source 16. All these values statistically agree, on average, with the result reported by Ledlow & Owen (1995).

This is also consistent with the offset of ∼100 kpc, typically found between the optical and the X-ray cluster centroids (Dai et al. 2007). Furthermore (as pointed out in Section 1), at variance with FR II radio galaxies or other types of AGNs, low-redshift FR Is are typically hosted by undisturbed ellipticals or cD galaxies (Zirbel 1996), which are often associated with the BCGs (von der Linden et al. 2007). To the best of our knowledge, the bright BCG discovered by Liu et al. (2013) at $z = 1.1$ is the most distant cD galaxy confirmed to date. Therefore, in light of the results presented here, the hosts of our FR Is could also constitute a sample of high-z cD galaxy candidates.

Concerning the BCGs, previous work found that they preferentially reside within $\lesssim$41 kpc from the X-ray cluster center up to $z \simeq 1$ (Semler et al. 2012). However, Zitrin et al. (2012)

found that the offset, if estimated from the optical cluster centroid, increases for increasing redshifts (i.e., up to ∼14 kpc at $0.52 < z < 0.55$). A similar trend is not excluded for our cluster candidates. In fact, we find that six of our cluster candidates are detected within an annulus centered at the coordinates of the radio galaxy and an internal radius of $\gtrsim$50 arcsec (see also Table 2 and related discussion in Section 6.4). Note that 50 arcsec correspond to 427 kpc at redshift $z = 1.5$. These six overdensities correspond to 32% ± 11% of our 19 cluster candidates.[17]

The six sources are the LLRGs 26, 29, and 285 and the HLRGs 34, 37, and 226. Although the statistics is extremely poor, this result implies that half of the sample of the HLRGs show significant offsets (i.e., $\geqslant$50 arcsec), while a non-null offset occurs for only ∼20% of the LLRGs. However, based on such a small sample we do not draw firm conclusions.

In order to investigate the marginal discrepancy found between the two subsamples, it would be interesting (1) to look for FR I radio galaxies in COSMOS at redshifts similar to those of the HLRGs, but with radio powers comparable with those of the LLRGs, and (2) to search for radio galaxies with redshifts similar to those of LLRGs and radio powers comparable with those of the HLRGs. This will improve the sample statistics and will allow us to understand if the trend is due either to evolutionary properties (being the LLRGs, on average, at lower redshifts than the HLRGs) or to the difference in radio power between the LLRGs and the HLRGs.

A possibility is that such radio galaxies are hosted in underdense regions within their cluster environment. To further investigate the above scenario we visually inspected the fields of the six sources. We did not find any evidence that the non-null offsets are present because of an artificiality or a technical bias of the I09 catalog (e.g., that some sources at the redshift of the cluster candidate and in the field of the corresponding FR I are not included in the I09 catalog or that their redshifts are erroneously estimated). We also found that the galaxies in each of these fields at redshifts around that of the corresponding FR I are homogeneously distributed around the position of the radio galaxy. This means that, although these overdensities are detected with significant offsets from the location of the corresponding FR I, each radio source is still likely located around the barycentric center of the galaxies in the field, in the projected sky, and not in the outskirts of the cluster candidate.

Furthermore, our results could also imply that our cluster candidates are still encompassing a strong evolution in terms of the spatial segregation of the galaxies within the core (see, e.g., Bassett et al. 2013, for a very detailed study about a $z \sim 1.6$ forming cluster).

8.9. A Bright Arc in the Field of 01

In this section we discuss the serendipitous discovery of a bright arc detected with the ACS camera on board *HST* in the field of source 01, at $z_{\rm spec} = 0.88$. In Figure 12 we report the ACS image (Koekemoer et al. 2007) of the field of 01. Source 01 and the arc are marked in the figure with the left and the right ellipses, respectively.

The arc is clearly visible about ∼5 arcsec westward of the pair formed by the radio galaxy host and a larger elliptical companion. Such a projected angular separation corresponds to ∼39 kpc at the redshift of the source. The arc is very close to the radio galaxy, and it resides within the core of the megaparsec-scale overdensity associated with source 01.

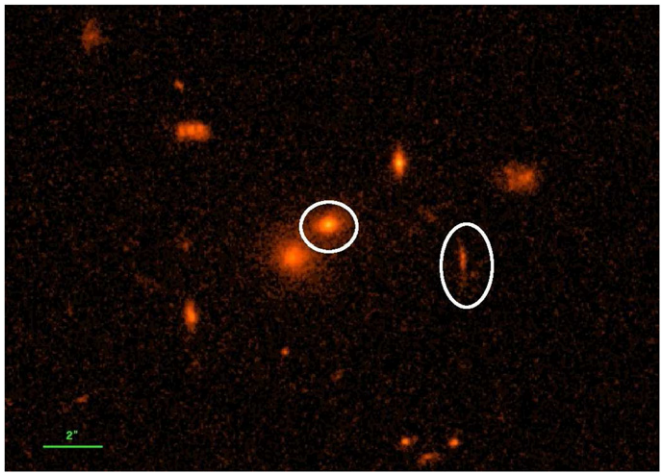

Figure 12. Field ($22'' \times 16''$ dimension) of source 01 as observed by ACS on board *HST* (Koekemoer et al. 2007). The host galaxy of source 01 and the bright arc are marked with the left and right ellipses, respectively.
(A color version of this figure is available in the online journal.)

Strong lensing phenomena are expected to be originated close to the densest regions of dark matter halos. Since such a projected separation is consistent with the typical size (i.e., ∼60 kpc; Halkola et al. 2007) of the dark matter halos of BCGs, it is likely that the arc originated from the dark matter halo of the galaxy pair.

An alternative scenario is motivated by the fact that the overdensity associated with source 01 is a relatively compact rich group with an estimated core size of about 70 arcsec (as suggested by Finoguenov et al. 2007; George et al. 2011; Knobel et al. 2012, and in this work). Therefore, it is also possible that the group halo itself is responsible for the observed effect. In fact, groups with intermediate masses in the range 10^{12}–$10^{14}\ M_{\odot}$ are usually more massive than galactic halos and concentrated enough to act as lenses (More et al. 2012).

The I09 catalog reports a photometric redshift $z = 0.715$ for the arc. However such a redshift is significantly lower than that of 01. This is unexpected, since the dark matter halo should be located between the observer and the lensed object. In order to understand the discrepancy we visually inspected the COSMOS archival images of the field at different wavelengths, roughly between the *i* and the *u* bands. In Figure 13 we report four images ($10'' \times 10''$ each) of the field of the arc, which is clearly marked with a green circle in each of them.

We find that the arc is very bright from the F814W filter to the *B*-band, but it completely disappears in the u^*-band. Therefore, we suspect that this is a *u*-band drop out and that the source associated with the arc is located at redshift $z \simeq 2.3$ or even higher.

While the arc clearly disappears in the *u*-band image, a close companion SW of the arc is clearly visible in all four images. We suspect that, during their automatic procedure, I09 erroneously associated with the bright arc the u^*-band flux measurement that corresponds to this companion. This likely leads to an incorrect photometric redshift estimate.

Hence, our serendipitous discovery suggests that this project might also be promising for systematic studies of (strong) lensing features observed in rich groups or clusters. Our method might be complementary and would extend to higher redshifts projects that find rich groups on the basis of strong lensing

[17] Note that for this case we consider 19 clusters because for the purpose of estimating sizes of clusters and locations of the FR I beacons we exclude multiple overdensities within the same field (see Section 6.6).

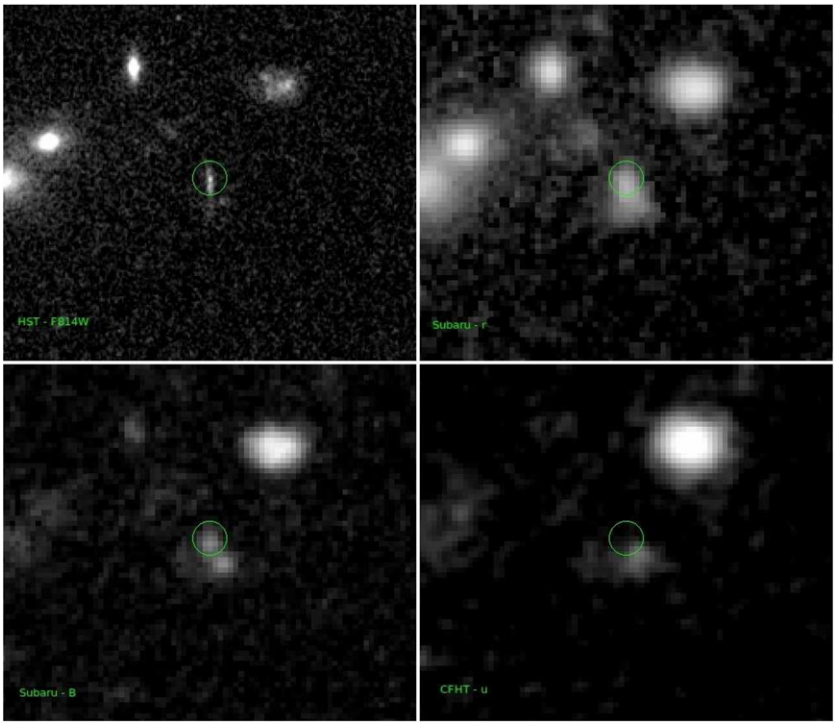

Figure 13. Images ($10'' \times 10''$ dimension) of arc located in the field source 01 approximately from *i*- to *u*-bands. The arc is marked with a green circle in the center of each image. Top left: *HST*/ACS image (F814W filter, Koekemoer et al. 2007). Top right: Subaru r^+−band. Bottom left: Subaru *B* band (Taniguchi et al. 2007). Bottom right: u^* Canada–France–Hawaii Telescope image (Capak et al. 2007).

(A color version of this figure is available in the online journal.)

signatures (e.g., Cabanac et al. 2007; Limousin et al. 2009; More et al. 2012).

One limitation of such searches is that lensing features are less likely at increasing redshifts. This is mainly because the projected number density of background objects decreases as the redshift of the lens increases. This has so far limited the number of high-redshift groups detected by means of strong lensing phenomena to $z \lesssim 1.2$. Similarly, we expect to have a better chance of observing possible occurrence of lensing phenomena for our $z \simeq 1$ cluster candidates than at higher redshifts. Therefore, our sample might not include a large number of strongly lensed objects while it includes an extremely useful number of high-redshift groups.

8.10. The Nature of the HLRGs

HLRGs represent the class of relatively higher power radio galaxies in our sample. As discussed in Section 3 and clearly shown in Figure 5, such sources have radio power slightly above the formal FR I/FR II radio power divide. Furthermore, the possible presence of bimodality in the radio power distribution of FR Is in our sample suggests that HLRGs might be drawn from a different parent population (see Section 3.6). In this section we will discuss the properties of HLRGs with respect to their radio properties.

Radio galaxies with clear FR II morphology (i.e., which showed evidence of clearly separated hot spots) were rejected during the C09 sample selection procedure. This immediately excludes the possibility that the HLRGs might be classical FR II radio sources based on their radio morphology.

8.10.1. Radio Galaxies of Transitional Type

A possible scenario is that HLRGs are radio galaxies of transitional type, i.e., with radio morphology typical of FR I sources and radio power typical of the local faint FR II radio galaxy population. This is not surprising because the high-power tail of the FR I radio power distribution partially overlaps with the low luminosity tail of the FR IIs, at least at low redshifts.

Furthermore, it has been proposed that the classical FR I/FR II radio luminosity divide undergoes a positive evolution with increasing redshift (e.g., Heywood et al. 2007). In such a scenario, radio galaxies with radio morphology typical of FR I sources and radio power typical of local FR IIs would be more common at the redshifts of our interest than at low-intermediate redshifts.

8.10.2. Compact Radio Sources

As discussed in C09, the rejection of radio galaxies with clear FR II morphology was first performed based on the FIRST survey (Becker et al. 1995), and then by using the VLA-COSMOS survey (Schinnerer et al. 2007). Their radio maps have typical resolutions of ∼5 arcsec (FIRST) and ∼1.5 arcsec (VLA-COSMOS), which correspond to 43 kpc and 13 kpc, at redshift $z = 1.5$, respectively. This selection excludes the presence of classical FR IIs in the sample, since the radio jets of these sources typically extend to distances larger than ∼a few tens of kpc, up to the megaparsec scale.

Almost all of the LLRGs and all of the HLRGs are observed as compact radio sources in both the FIRST and the VLA-COSMOS surveys. As pointed out in C09, there are two possible scenario. (1) While the core has a flat radio spectrum, the extended emission of radio sources has a steep spectrum. Because of the light redshifting, the extended emission is therefore increasingly more difficult to detect at increasing redshifts. Therefore, it might be that both the FIRST and the VLA-COSMOS surveys detect the core emission only. (2) Alternatively, the radio galaxies in our sample are intrinsically

small. The first scenario was discussed in C09. Therefore, we limit our discussion to the second possibility.

If the sources in our sample are intrinsically compact, they are entirely contained within a few ∼10 kpc scale. They might show a radio morphology somehow different from that of classical FR Is. If this is the case we suggest that the HLRGs might be Compact Steep Spectrum (CSS) sources (e.g., Saikia 1988; Fanti et al. 1990; Fanti & Fanti 1994; Dallacasa et al. 1993; Fanti & Spencer 1995) or GHz Peaked Spectrum (GPS; e.g., O'Dea et al. 1991) sources.

The GPS are commonly contained within the narrow line region at the $\lesssim$1 kpc scale, while the CSS sources are usually contained within the host galaxy (i.e., $\lesssim$15 kpc). They would not be resolved at redshift $z \gtrsim 1$ by using the VLA-COSMOS and the FIRST surveys. Therefore, the possibility that some of the HLRGs are GPS or CSS cannot be excluded.

The GPS and CSS sources show a complex multiple radio morphology (see also O'Dea 1998, and references therein for a review). They are preferentially found at lower redshifts ($z \lesssim 1$ Fanti et al. 1990; O'Dea et al. 1991), and have higher radio powers (i.e., ∼2 orders of magnitude brighter, O'Dea & Baum 1997) than those of HLRGs. This also implies that the presence of GPS or CSS sources within HLRGs is more likely than for LLRGs.

However, the radio powers of the FR Is in our sample (including both LLRGs and HLRGs) are fully consistent with those of local faint radio sources studied by Drake et al. (2004). Most of the galaxies in their sample are compact and therefore resemble CSS or GPS sources. They have redshifts and low frequency radio luminosities between $z \simeq 0.05$–0.35 and $L_{1.4} \simeq 31.0$–$34.2\,\mathrm{erg\,s^{-1}\,Hz^{-1}}$, respectively. Interestingly, this suggests that all of the radio galaxies in our sample might be similar to the local radio sources in the Drake et al. (2004) catalog.

If some of our sources were confirmed to be CSSs or GPSs, they would constitute a population of compact radio sources with higher redshifts and lower radio power than those included in previous samples of intermediate redshift objects of these two classes (e.g., Dallacasa et al. 1995, 1998, 2013).

It would be interesting to study the spectral properties of the HLRGs in our sample with multiwavelength radio observations to see if they are consistent with the steep spectra typical of CSS or if the SEDs are instead consistent with those of GPS sources that show a peak at high radio frequencies. High angular resolution ($\lesssim$0.1 arcsec) radio observations with the very long baseline interferometry network may allow us to investigate in detail the radio morphology of these sources.

According to the theoretical evolutionary scenario suggested for CSSs and GPSs by Snellen et al. (2000), if the radio galaxies in our sample are compact $\gtrsim$1 kpc sources, they will evolve into classical FR Is increasing their size and decreasing their radio luminosity. Alternatively, if our sources are $\lesssim$1 kpc GPSs, they will increase their luminosities and sizes, until they reach a ∼1 kpc size. Then, they will decrease their radio power, evolving into CSSs and finally into radio galaxies.

Conversely, Tinti & De Zotti (2006) found observational evidence that GPS sources always evolve by decreasing their luminosity and increasing their size. This is in agreement with the theoretical model suggested by Begelman (1996).

Therefore, it might be that, during their evolution, some of our sources will reach a higher radio power. However, it is unlikely that they will increase their radio luminosities enough to evolve into radio galaxies with a radio morphology typical of classical FR IIs, as also suggested by Drake et al. (2004) for their sample of lower redshifts compact sources.

9. CONCLUSIONS AND FUTURE WORK

We applied a newly developed method to search for overdensities around the $z \sim 1$–2 FR Is of the C09 sample, which has been accurately redefined in this work. We found that the great majority of the FR Is in the sample reside in megaparsec-scale rich groups or clusters. We estimated, for each cluster candidate: (1) detection significance, (2) redshift, (3) size, and (4) richness.

We also compared our results with those obtained by previous works on the environments of low redshift radio galaxies, high-redshift FR IIs, and cluster samples at intermediate redshifts. The fraction of FR Is that are associated with cluster environments in our redshift range is consistent with that found for low redshift (i.e., $z \leqslant 0.25$) FR Is. However, it is significantly higher than that found for both local and high-redshift FR IIs.

Moreover, we applied an independent method based on IR colors to search for high-redshift overdensities (Papovich 2008, P08) by performing a counts-in-cell analysis. Interestingly, all six cluster candidates that are found with such a method are also detected by the PPM. Conversely, the great majority (i.e., ∼70%) of our $z \gtrsim 1.3$ cluster candidates are not found by the P08 method. Since the P08 method is applied performing a counts-in-cell analysis, some of the clusters that are not detected by the P08 method might be populated by galaxies that are not completely segregated in the cluster core.

Spectroscopic confirmations and detailed multiwavelength observations of our cluster candidates are nevertheless required to study them in more detail to confirm the results obtained in this work. This is especially important for our high-redshift ($z \gtrsim 1.5$) cluster candidates. These would significantly increase the statistics of cluster samples at such high redshifts and might allow a more complete understanding of the ongoing processes involved in the formation and the evolution of these structures.

In more detail, it would be interesting to observe the cluster candidates with deeper IR and optical observations to look for any evidence (or absence) of the red sequence or a segregation of faint red objects in the fields that we might be missing by using the COSMOS catalog (Ilbert et al. 2009). Rest frame ultra-violet (UV) observations might also help us search for the possible presence of Lyα emitting regions that are commonly found in $z \gtrsim 2$ protoclusters. X-ray observations deeper than those available within the COSMOS survey will allow us to search for signatures of hot plasma within the ICM (Tundo et al. 2012). All of these observations will help establish whether our clusters are still evolving. Alternatively, they might exhibit transitional properties between those typical of high-redshift ($z > 2$) Lyα emitter protoclusters and those associated with low redshift clusters that show common features such as X-ray emission, red-sequence, and segregation of red objects within the core.

In general, our results suggest that the megaparsec-scale overdensities associated with the radio galaxies in our sample are similar, independent of the two subclasses considered throughout this work (i.e., the LLRGs and the HLRGs), in terms of estimated richness, mass, and size. Interestingly, on the basis of their multi-component SED fitting, Baldi et al. (2013) also found that the host galaxies of both low- and high-power radio galaxies in the C09 sample have homogeneous properties, in terms of UV and IR luminosities, stellar mass content, and dust temperature, independent of the subsample

considered. Therefore, we can conclude that the radio galaxies in the C09 sample constitute a homogeneous population.

Furthermore, we reported the serendipitous discovery of a bright arc in the field of 01, which is at $z_{\rm spec} = 0.88$. This might suggest that the cluster associated with that source is rich and compact (as suggested by Finoguenov et al. 2007; George et al. 2011; Knobel et al. 2012, and in this work). The presence of strong and weak lensing features in our sample might be present for some of our cluster candidates. We will investigate this scenario in a forthcoming paper.

The above results, combined with the steepness of the radio luminosity function of the radio galaxies, suggest that low power FR Is are more effective than FR IIs as beacons to search for groups and clusters at high redshifts.

Radio sources with radio powers typical of those of our FR Is are found only in 10%–20% of X-ray- and optically selected clusters at $z \lesssim 1$ (Branchesi et al. 2006; Gralla et al. 2011). Therefore, unless this percentage dramatically changed at $z \geqslant 1$ we might still be missing 80%–90% of the entire cluster population at the redshifts of our interest. It would be interesting to blindly apply the PPM to the entire COSMOS field to robustly estimate the total number of overdensities. This will allow us to compare that with the number counts predicted by the ΛCDM model. We will investigate these aspects in a future work.

Interestingly, our cluster candidates might be also studied by using next generation telescopes such as *James Webb Space Telescope*. Although the PPM is primarily introduced for the COSMOS survey, it may be applied to wide field surveys to blindly search for cluster candidates by using accurate photometric redshift information. In particular, we will also extend our work to wider surveys (e.g., stripe 82 of the SDSS), where we expect to find a higher number of both FR Is (∼3000) and cluster candidates (∼2100). Furthermore, we will have a higher chance of finding more massive structures and lensing phenomena. Two possible limitations are that the FR Is are difficult to find and that the PPM requires good photometric redshifts. Moreover, our method will be less effective for those surveys that will provide sufficient spectroscopic high-redshift information, where standard three-dimensional methods (e.g., correlation functions) might be more successfully applied.

Conversely, the PPM might also be applied to future wide field surveys such as LSST and *Euclid* which will provide good photometric redshift information. Another possible use of the PPM is a search for (proto-)clusters at $z \gtrsim 2$ by adopting radio galaxies or other sources (e.g., Lyman break galaxies) as beacons.

The careful selection of our FR I sample and the accurate redshift estimates have also allowed us to estimate the comoving space density of sources with $L_{1.4} \simeq 10^{32.3}\,{\rm erg\,s^{-1}\,Hz^{-1}}$ at $z \simeq 1.1$. Previous direct observational estimates and model predictions span a quite broad range. Our result is consistent with the upper values and strengthens the case for a strong cosmological evolution of these sources.

We thank the anonymous referee for helpful comments. We thank the Space Telescope Science Institute, where part of this work was developed. We also thank Roberto Gilli, Piero Rosati, and Paolo Tozzi for fruitful discussion. This work was partially supported by the STScI JDF account D0101.90157 and (G.C.) by both the Internship Program ISSNAF-INAF 2010 and one of the Foundation Angelo Della Riccia fellowships both in 2012 and in 2013. This research has made use of the NASA/IPAC Extragalactic Database (NED) which is operated by the Jet Propulsion Laboratory, California Institute of Technology, under contract with the National Aeronautics and Space Administration.

REFERENCES

Adami, C., Durret, F., Benoist, C., et al. 2010, A&A, 509A, 81
Adami, C., Durret, F., Guennou, L., & Da Rocha, C. 2013, A&A, 551, A20
Adami, C., Mazure, A., Pierre, M., et al. 2011, A&A, 526, 18
Alberts, S., Pope, A., Brodwin, M., et al. 2014, MNRAS, 437, 437
Allen, S. W., Evrard, A. E., & Mantz, A. B. 2011, ARAA, 49, 409
Ashman, K. M., Bird, C. M., & Zepf, S. E. 1994, AJ, 108, 2348
Bahcall, N. A., Dong, F., Hao, L., et al. 2003, ApJ, 599, 814
Baldi, T., Chiaberge, M., Capetti, A., et al. 2013, ApJ, 762, 30B (B13)
Banerji, M., Chapman, S. C., Smail, I., et al. 2011, MNRAS, 418, 1071
Barone-Nugent, R. L., Wyithe, J. S. B., Trenti, M., et al. 2013, arXiv:1303.6109
Bassett, R., Papovich, C., Lotz, J. M., et al. 2013, ApJ, 770, 58
Becker, R. H., White, R. L., & Helfand, D. J. 1995, ApJ, 450, 559
Begelman, M. C. 1996, in Cygnus A: Study of a Radio Galaxy, ed. C. L. Carilli & D. A. Harris (Cambridge: Cambridge Univ. Press), 209
Benson, B. A., de Haan, T., & Dudley, J. P. 2013, ApJ, 763, 147
Bode, P., Bahcall, N. A., Ford, E. B., & Ostriker, J. P. 2001, ApJ, 551, 15
Böhringer, H., Schuecker, P., Guzzo, L., et al. 2004, A&A, 425, 367
Branchesi, M., Gioia, I. M., Fanti, C., et al. 2006, A&A, 446, 97
Brodwin, M., Gonzalez, A. H., Stanford, S. A., et al. 2012, ApJ, 753, 162
Brodwin, M., Stanford, S. A., Gonzalez, A. H., et al. 2013, ApJ, 779, 138
Brodwin, M., Stern, D., Vikhlinin, A., et al. 2011, ApJ, 732, 33
Cabanac, R. A., Alard, C., Dantel-Fort, M., et al. 2007, A&A, 461, 813
Capak, P., Aussel, H., Ajiki, M., et al. 2007, ApJS, 172, 99
Capak, P. L., Riechers, D., Scoville, N. Z., et al. 2011, Natur, 470, 233
Casasola, V., Magrini, L., Combes, F., et al. 2013, A&A, 558, 60
Castignani, G., Chiaberge, M., Celotti, A., & Norman, C. 2014, ApJ, 792, 113 (Paper I)
Cavaliere, A., & Fusco-Fermiano, R. 1978, A&A, 70, 677
Chiaberge, M., Capetti, A., & Celotti, A. 1999, A&A, 349, 77
Chiaberge, M., Capetti, A., Macchetto, F. D., et al. 2010, ApJL, 710, L107 (C10)
Chiaberge, M., Tremblay, G., Capetti, A., et al. 2009, ApJ, 696, 1103 (C09)
Chiang, Y.-K., Overzier, R., & Gebhardt, K. 2013, ApJ, 779, 127
Condon, J. J., Cotton, W. D., Greisen, E. W., et al. 1998, AJ, 115, 1693
Cooray, A., & Sheth, R. 2002, PhR, 372, 1
Cruddace, R., Voges, W., Böhringer, H., et al. 2002, ApJS, 140, 239
Dai, X., Kochanek, C. S., & Morgan, N. D. 2007, ApJ, 658, 917
Dalal, N., White, M., Bond, J. R., & Shirokov, A. 2008, ApJ, 687, 12D
Dallacasa, D., Bondi, M., Alef, W., & Mantovani, M. 1998, A&AS, 129, 219
Dallacasa, D., Fanti, C., & Fanti, R. 1993, in Jets in Extragalactic Radio Sources, ed. H.-J. Roser & K. Meisenheimer (Heidelberg: Springer), 27
Dallacasa, D., Fanti, C., Fanti, R., Schilizzi, R. T., & Spencer, R. E. 1995, A&A, 295, 27
Dallacasa, D., Orienti, M., Fanti, C., Fanti, R., & Stanghellini, C. 2013, MNRAS, 433, 147
Davis, D. S., & Mushotzky, R. F. 1993, AJ, 105, 409
Diener, C., Lilly, S. J., Knobel, C., et al. 2013, ApJ, 765, 109
Donoso, E., Best, P. N., & Kauffmann, G. 2009, MNRAS, 392, 617
Donoso, E., Li, C., Kauffmann, G., et al. 2010, MNRAS, 407, 1078
Donzelli, C. J., Chiaberge, M., Macchetto, F. D., et al. 2007, ApJ, 667, 780
Drake, C. L., Bicknell, G. V., McGregor, P. J., & Dopita, M. A. 2004, AJ, 128, 969
Durret, F., Adami, C., Cappi, A., et al. 2011, A&A, 535A, 65
Eisenhardt, P. R. M., Brodwin, M., Gonzalez, A. H., et al. 2008, ApJ, 684, 905
Fanaroff, B. L., & Riley, J. M. 1974, MNRAS, 167, 31
Fanti, C., & Fanti, R. 1994, in ASP Conf. Ser. 54, The Physics of Active Galaxies, ed. G. V. Bicknell, M. A. Dopita, & P. J. Quinn (San Francisco, CA: ASP), 341
Fanti, R., Fanti, C., Schilizzi, R. T., et al. 1990, A&A, 231, 333
Fanti, R., & Spencer, R. E. 1995, in IAU Symp. 175, Extragalactic Radio Sources, ed. R. Ekers, C. Fanti, & L. Padrielli (Dordrecht: Kluwer), 63
Fassbender, R., Nastasi, A., Böhringer, H., et al. 2011, A&A, 527, 10
Finoguenov, A., Guzzo, L., Hasinger, G., et al. 2007, ApJS, 172, 182F
Galametz, A., Stern, D., De Breuck, C., et al. 2012, ApJ, 749, 169
Galametz, A., Stern, D., Pentericci, L., et al. 2013, A&A, 559, A2
George, M. R., Leauthaud, A., Bundy, K., et al. 2011, ApJ, 742, 125
Giavalisco, M. 2002, ARA&A, 40, 579
Gladders, M. D., & Yee, H. K. C. 2005, ApJS, 157, 1
Gobat, R., Daddi, E., Onodera, M., et al. 2011, A&A, 526, 133
Gobat, R., Strazzullo, V., Daddi, E., et al. 2013, ApJ, 776, 9
Gomez, P. L., Pinkney, J., Burns, J. O., et al. 1997, ApJ, 474, 580

Gralla, M. B., Gladders, M. D., Yee, H. K. C., & Barrientos, L. F. 2011, ApJ, 734, 103
Halkola, A., Seitz, S., & Pannella, M. 2007, ApJ, 656, 739
Hasselfield, M., Hilton, M., Marriage, T. A., et al. 2013, JCAP, 07, 008
Henry, J. P., Mullis, C. R., Voges, W., et al. 2006, ApJS, 162, 304
Heywood, I., Blundell, K. M., & Rawlings, S. 2007, MNRAS, 381, 1093
Hill, G. J., & Lilly, S. J. 1991, ApJ, 367, 1
Hinshaw, G., Weiland, J. L., Hill, R. S., et al. 2009, ApJS, 180, 225
Ilbert, O., Capak, P., Salvato, M., et al. 2009, ApJ, 690, 1236 (I09)
Jee, M. J., Dawson, K. S., Hoekstra, H., et al. 2011, ApJ, 737, 59
Jian, H.-Y., Lin, L., & Chiueh, T. 2014, ApJ, 788, 109
John, T. L. 1988, A&A, 193, 189
Knobel, C., Lilly, S. J., Iovino, A., et al. 2009, ApJ, 697, 1842
Knobel, C., Lilly, S. J., Iovino, A., et al. 2012, ApJ, 753, 121
Koekemoer, A. M., Aussel, H., Calzetti, D., et al. 2007, ApJS, 172, 196
Koyama, Y., Kodama, T., Tadaki, K., et al. 2014, ApJ, 789, 18
Kravtsov, A. V., & Borgani, S. 2012, ARA&A, 50, 353
Leauthaud, A., Finoguenov, A., Kneib, J.-P., et al. 2010, ApJ, 709, 97
Ledlow, M. J., & Owen, F. N. 1995, AJ, 109, 853
Ledlow, M. J., & Owen, F. N. 1996, AJ, 112, 9
Lilly, S. J., Le Fèvre, O., Renzini, A., et al. 2007, ApJS, 172, 70
Limousin, M., Cabanac, R., Gavazzi, R., et al. 2009, A&A, 502, 445
Liu, F. S., Guo, Y., Koo, D. C., et al. 2013, ApJ, 769, 147
Magliocchetti, M., & Brüggen, M. 2007, MNRAS, 379, 260
Mantz, A., Allen, S. W., Rapetti, D., & Ebeling, H. 2010, MNRAS, 406, 1759
Massardi, M., Bonaldi, A., Negrello, M., et al. 2010, MNRAS, 404, 532
Mauch, T., & Sadler, E. M. 2007, MNRAS, 375, 931
Mayo, J. H., Vernet, J., De Breuck, C., et al. 2012, A&A, 539A, 33
McAlpine, K., Jarvis, M. J., & Bonfield, D. G. 2013, MNRAS, 436, 1084
McIntosh, D. H., Wagner, C., Cooper, A., et al. 2014, MNRAS, 442, 533
Menci, N., Rosati, P., Gobat, R., et al. 2008, ApJ, 685, 863
Miley, G., & De Breuck, C. 2008, A&ARv, 15, 67
Mobasher, B., Capak, P., Scoville, N. Z., et al. 2007, ApJS, 172, 117
Mohr, J. J. 2005, in ASP Conf. Ser. 339, Observing Dark Energy, ed. S. C. Wolff & T. R. Lauer (San Francisco, CA: ASP), 140
More, A., Cabanac, R., More, S., et al. 2012, ApJ, 749, 38
Mortonson, M. J., Hu, W., & Huterer, D. 2011, PhRvD, 83, 023015
Muzzin, A., Wilson, G., Demarco, R., et al. 2013, ApJ, 767, 39
Nastasi, A., Fassbender, R., Böhringer, H., et al. 2011, A&A, 532, 6
Newman, A. B., Ellis, R. S., Andreon, S., et al. 2014, ApJ, 788, 51
Noble, A. G., Geach, J. E., van Engelen, A. J., et al. 2013, MNRAS, 436, 40
O'Dea, C. P. 1998, PASP, 110, 493
O'Dea, C. P., & Baum, S. A. 1997, AJ, 113, 148
O'Dea, C. P., Baum, S. A., & Stanghellini, C. 1991, ApJ, 380, 66
O'Dea, C. P., & Owen, F. N. 1986, ApJ, 301, 841
Papovich, C. 2008, ApJ, 676, 206 (P08)
Papovich, C., Momcheva, I., Willmer, C. N. A., et al. 2010, ApJ, 716, 1503
Peacock, J. A. 1999, Cosmological Physics (Cambridge: Cambridge Univ. Press)
Peebles, P. J. E. 1993, Physical Cosmology (Princeton, NJ: Princeton Univ. Press)
Planck Collaboration XX. 2013, arXiv:1303.5080
Planck Collaboration XXIX. 2013, arXiv:1303.5089
Prescott, M. K. M., Impey, C. D., Cool, R. J., & Scoville, N. Z. 2006, ApJ, 644, 100
Ramos Almeida, C., Bessiere, P. S., Tadhunter, C., et al. 2013, arXiv:1308.4725
Reichardt, C. L., Stalder, B., Bleem, L. E., et al. 2013, ApJ, 763, 127
Reiprich, T. H., & Böhringer, H. 1999, in Proc. of the Ringberg Workshop, Diffuse Thermal and Relativistic Plasma in Galaxy Clusters, ed. H. Bohringer, L. Feretti, & P. Schuecker (Garching: Max-Planck-Institut fur Extraterrestrische Physik), 157
Rigby, E. E., Best, P. N., & Snellen, I. A. G. 2008, MNRAS, 385, 310
Rigby, E. E., Hatch, N. A., Röttgering, H. J. A., et al. 2014, MNRAS, 437, 1882
Rosati, P., Borgani, S., & Norman, C. 2002, ARA&A, 40, 539
Rozo, E., Wechsler, R. H., Rykoff, E. S., et al. 2010, ApJ, 708, 645
Sadler, E. M., Cannon, R. D., Mauch, T., & Hancock, P. J. 2007, MNRAS, 381, 211
Saikia, D. J. 1988, in Active Galactic Nuclei, ed. H. R. Miller & P. J. Wiita (Berlin: Springer), 317
Sanders, D. B., Salvato, M., Aussel, H., et al. 2007, ApJS, 172, 86
Santos, J. S., Altieri, B., Popesso, P., et al. 2013, MNRAS, 433, 1287
Santos, J. S., Fassbender, R., Nastasi, A., et al. 2011, A&A, 531, 15
Schinnerer, E., Smolcic, V., Carilli, C. L., et al. 2007, ApJS, 172, 46
Schmidt, M. 1968, ApJ, 151, 393
Scoville, N., Arnouts, S., Aussel, H., et al. 2013, ApJS, 206, 3
Scoville, N., Aussel, H., Benson, A., et al. 2007a, ApJS, 172, 150
Scoville, N., Aussel, H., Brusa, M., et al. 2007b, ApJS, 172, 1
Semler, D. R., Suhada, R., Aird, K. A., et al. 2012, ApJ, 761, 183
Sheth, R. K., & Tormen, G. 2004, MNRAS, 350, 1385
Smith, E. P., & Heckman, T. M. 1990, ApJ, 348, 38
Smolčić, V., Finoguenov, A., Zamorani, G., et al. 2011, MNRAS, 416, 31
Smolčić, V., Zamorani, G., Schinnerer, E., et al. 2009, ApJ, 696, 24
Snellen, I. A. G., Schilizzi, R. T., Miley, G. K., et al. 2000, MNRAS, 319, 445
Spitler, L. R., Labbé, I., Glazebrook, K., et al. 2012, ApJL, 748, L21
Stanford, S. A., Brodwin, M., Gonzalez, A. H., et al. 2012, ApJ, 753, 164
Steidel, C. C., Adelberger, K. L., Shapley, A. E., et al. 2000, ApJ, 532, 170
Steidel, C. C., Shapley, A. E., Pettini, M., et al. 2004, ApJ, 604, 534
Strazzullo, V., Gobat, R., Daddi, E., et al. 2013, ApJ, 772, 118
Šuhada, R., Song, J., Böhringer, H., et al. 2012, A&A, 537A, 39
Sunyaev, R. A., & Zel'dovich, Ya. B. 1972, CoASP, 4, 173
Tanaka, M., Finoguenov, A., Mirkazemi, M., et al. 2013, PASJ, 65, 17T
Taniguchi, Y., Scoville, N., Murayama, T., et al. 2007, ApJS, 172, 9
Tinker, J., Kravtsov, A. V., Klypin, A., et al. 2008, ApJ, 688, 709
Tinti, S., & De Zotti, G. 2006, A&A, 445, 889
Tozzi, P., Santos, J. S., Nonino, M., & Rosati, P. 2013, A&A, 551A, 45
Trump, J. R., Impey, C. D., McCarthy, P. J., et al. 2007, ApJS, 172, 383
Tundo, E., Tozzi, P., & Chiaberge, M. 2012, MNRAS, 420, 187
Venemans, B. P., Röttgering, H. J. A., Miley, G. K., et al. 2007, A&A, 461, 823
Venturi, T., Castaldini, C., Cotton, W. D., et al. 1995, ApJ, 454, 735
Vikhlinin, A., Kravtsov, A. V., Burenin, R. A., et al. 2009, ApJ, 692, 1060
von der Linden, A., Best, P. N., & Kauffmann, G. 2007, MNRAS, 379, 867
Weinberg, D. H., Mortonson, M., Eisenstein, D., et al. 2013, PhR, 530, 87
Wen, Z. L., & Han, J. L. 2011, ApJ, 734, 68
Willott, C. J., Rawlings, S., Blundell, K. M., Lacy, M., & Eales, S. A. 2001, MNRAS, 322, 536W (W01)
Wing, J. D., & Blanton, E. L. 2011, AJ, 141, 88
Worpel, H., Brown, M. J. I., Jones, D. H., Floyd, D. J. E., & Beutler, F. 2013, ApJ, 772, 64
Wylezalek, D., Galametz, A., & Stern, D. 2013, ApJ, 769, 79
Zatloukal, M., Röser, H.-J., Wolf, C., Hippelein, H., & Falter, S. 2007, A&A, 474, 5
Zeimann, G., Stanford, S. A., Brodwin, M., et al. 2013, ApJ, 779, 137
Zeimann, G. R., Stanford, S. A., Brodwin, M., et al. 2012, ApJ, 756, 115Z
Zirbel, E. L. 1996, ApJ, 473, 713
Zirbel, E. L. 1997, ApJ, 476, 489
Zitrin, A., Bartelmann, M., Umetsu, K., Oguri, M., & Broadhurst, T. 2012, MNRAS, 426, 2944